OUTLINE AND APPLICATION OF THE NLR AEROELASTIC SIMULATION METHOD *

M.H.L. Hounjet [†]and B.J.G. Eussen [‡]

National Aerospace Laboratory (NLR),

Anthony Fokkerweg 2,

1059 CM Amsterdam,

The Netherlands

Abstract

The NLR system for the transonic aeroelastic analysis of complete aircraft is presented. The aerodynamic part of the method which is primarily based on the full potential equation is described and attention is given to a consistent start of the applied Newton subiteration process. Methods which take care of the transfer of aeroelastic data are described, including the extension of the surface spline method to a volume spline method. The method is demonstrated by showing results of unsteady loads and pressure coefficients applications in 3-D subsonic flow and of aeroelastic applications to a 3-D AGARD standard aeroelastic case and a supercritical wing in transonic flow.

Nomenclature

Abbrev.	Description
AF	approximate factorisation
AESIM	aeroelastic simulation method for transport type aircraft
CAR	unsteady full body panel method for arbitrary configurations
FTRAN3	unsteady transonic field panel method for wings
LMS	Leuven measurement systems
GUL	unsteady lifting surface method for arbitrary configurations
NASTRAN	NASA structural analysis FEM package
PK	solution method for aeroelastic eigenvalue problem

Roman	description
a	speed of sound $a^2 = \gamma \frac{p}{\rho}$
(a, b, c, d, e)	coefficients of surface and volume spline method
C_p	pressure coefficient
D	Damping matrix
d	modified mass matrix
dcp	pressure difference through lifting surface
f	freestream mass flux correction
F, f	aerodynamic force vector
g	damping ratio (% crit.)
H	Jacobian transformation matrix
IM	denotes imaginary part
J, j	Jacobian of $H, j = \frac{1}{J}$
h	virtual body displacements (vibrations)
k	reduced frequency, $k = \frac{\omega l}{V_\infty}$
K, k	stiffness matrix
l	reference length
L	linear equations (operators, Jacobians)
M	Mach number
M	mass matrix
$\vec{n}$	disturbance normal
$\vec{N}$	normal vector
p	pressure
q	dynamic pressure
$\vec{q}$	velocity
q_i	i^{th} generalized coordinate
Q_i	i^{th} modified generalized coordinate
$\dot{q}_i$	i^{th} generalized velocity
$\vec{Q}$	contravariant velocity
$\vec{r}$	position vector
R	gas constant, $c_p - c_v$
$\vec{R}$	compressible position vector
RE	denotes real part
Res	residual equations
S	entropy

t	time
T	modified time
u, v, w	velocities in x,y and z direction, respectively
U, V, W	contravariant velocities in ξ, η and ζ direction, respectively
V	control volume in hyperbolic grid generation
xy	symmetry plane $z = 0$
xz	symmetry plane $y = 0$
x, y, z	Cartesian coordinates

Subscripts superscripts	Description
a	denotes absorbing condition
b	denotes body
f	denotes far field
m	denotes mass flux condition
n	last time station, referring to n^{th} time step
$n+1$	next time station, referring to $(n+1)^{th}$ time step
s	denotes shock wave
T	transpose
w	wake
$\heartsuit$	last updated state $(n + 1)$ approximation
∞	far upstream
$\star$	unnormalized normal
$*$	intermediate result, sonic reference state

Greek and others	Description
α	angle-of-attack
γ	ratio of specific heats $\frac{c_p}{c_v}$ (1.4 for diatomic gas)
θ	control angle in hyperbolic grid generation
ζ	curvilinear coordinate in axial direction
η	curvilinear coordinate in circumferential direction
ϕ	potential
φ	control angle in hyperbolic grid generation
κ	lumping parameter
ξ	curvilinear coordinate in freestream direction
ρ	density
$\vec{\sigma}$	grid displacement
τ	modified time
Υ	Clebsch potential
$\triangle\#$	mesh spacing
$\triangle\tau$	time step
$\vec{\nabla}$	gradient
$\overleftarrow{\nabla}$	upwind gradient

$\overleftarrow{\#}$	upwind operator, quantity
$\overleftrightarrow{\#}_Q$	upwind or downwind operator depending on Q
$\sqsubset\#\sqsupset$	$\#^{upper} - \#^{lower}$ at slits or $\#^{upwind} - \#^{downwind}$ at shock waves
$\#$	variable

Introduction

After the successful acceptance by the aircraft industry of the Doublet Lattice method [1] in the sixties for lifting surfaces in subsonic flow, followed two decades later by the Constant Pressure Panel method [2, 3] for lifting surfaces in supersonic flow, the development of methods for the transonic flow regime which can be applied with comparable efficiency, reliability, low cost and ease of usage are still needed.

Thus far many methods have been introduced by researchers for the transonic flow domain which in one way or the other will not be readily accepted by aircraft industry due to shortcomings in modeling, efficiency, cost and/or ease of usage. Examples are restrictions to single wings, too advanced modelings (Euler + TLNS + unstructured grids), separated pre- and postprocessings (grid generation and signal analysis) and no interface with NASTRAN. Another reason for the hesitation of industry seems to be the difficulties involved in surface grid generation, flow field grid generation, time domain analysis and in representing the elastomechanical data on the aerodynamic surface.

A similar observation concerns unsteady subsonic and supersonic panel methods modeling complete aircraft configurations as thick bodies, which introduce additional work with respect to the lifting surface methods in panel generation, represention of the vibration modes on the panels and in inspection.

The latter seems to be the primary cause that limited use has been made by industry. Besides, a very limited number of panel methods exist that deal with the unsteady flow about complete aircraft.

At NLR full aircraft modeling panel methods have reached the status desrcibed in [3], with the CAR and GUL methods as results. The CAR method is capable of modeling a complete oscillating aircraft (with thin and thick wings) in subsonic and supersonic flow and supports Hounjet's diverging rate approach [4, 5, 6] with which generalized forces can be obtained very efficiently by avoiding complex arithmetics. The GUL method is the equivalent lifting surface method. Since then only minor changes have been made to these methods.

On the basis of direct (simultaneous solution of the equations of unsteady aerodynamics and elastomechanical equations) simulation of unsteady transonic flow about a flexible aircraft the development of a

method has nearly been completed which aims at reducing the aforementioned drawbacks. The method is called AESIM (aeroelastic simulation). The full potential model has been adopted as the building stone of the aerodynamic part of the method, completed with the Clebsch potential to account for shock-induced entropy and vorticity effects [7]. The feasibility of direct simulation was demonstrated by a comparable development at Rockwell [8] and at NASA-Langley [9].

This approach offers the possibility to predict aeroelastic quantities of interest (flutter boundaries, unsteady loads, stability derivatives, gust loads and fatigue spectra) within acceptable turn-around times on current state-of-the-art workstations which allow fast direct visual monitoring and analysis and which provide the computer power (> 100 dMFLOPS) needed for routine simulation.

In an early stage of the development it was decided to develop and integrate surface grid generation, grid generation, elastomechanical interpolation, analysis and visualisation methods from requirements within the aeroelasticity branches at NLR and Fokker Aircraft B.V. and **not** from pushing factors from the CFD community.

At the same time the full aircraft modeling panel methods, once integrated, will benefit from this development due to the especially developed surface grid generation tools, the elastomechanical interpolation tools , the visualisation tools and the NASTRAN interface.

This paper presents important aspects of the status of the aeroelastic simulation environment and discusses results of applications in unsteady 3-D flow.

Aeroelastic Simulation System

Figure 1 presents the environment which is under development at NLR and this section presents briefly the important components of the target aeroelastic simulation method. It should be noted that some of the parts mentioned here are in the process of development.

The various elements of this environment will now be discussed in more detail.

Surface grid generation

With respect to aeroelastic requirements only the substructures of aircraft which are slender and have surfaces with low curvature (wing, tail and fin) need to be modelled quite well in obtaining the aerodynamic force in normal direction. Therefore the interference effects of the fuselage and blunt-nosed parts should be
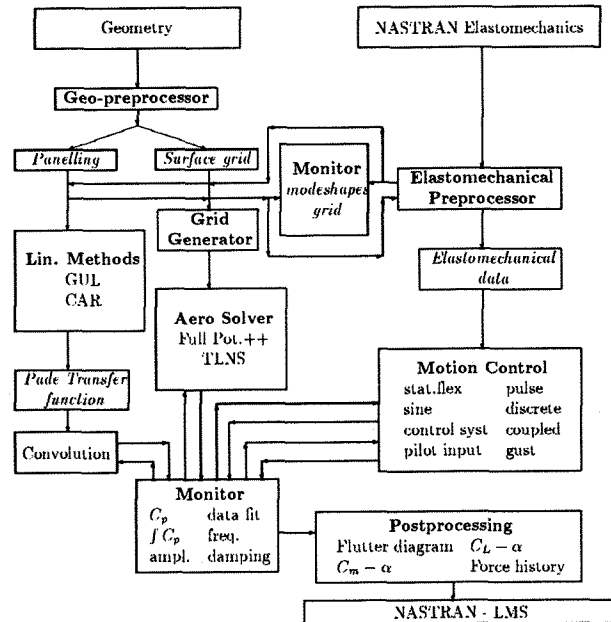

Figure 1: Aeroelastic Simulation Environment

modelled properly without the need to obtain very accurate results at those relatively small parts, since the contribution of drag forces to aeroelastic characteristics is generally limited. Consequently the quality and density of the surface grids can be relaxed in these areas. While the aeroelastician is not expected to be an expert surface modeler who creates a surface grid from scratch, the assumption is made that an initial surface grid is available which can be tuned to his needs in routine applications by a geometry preprocessor. The geometry preprocessor generates a mono-block structured surface description and/or paneling of the complete aircraft with embedded upwind slits and downwind slits (wake surfaces) by assembling separate airframe components (provided by the user by means of other programs). It also constructs the slits, allows for redistributions, data editing, data smoothing and stripping and tailors the configuration to aeroelastic needs. By this, considerable flexibility is offered to the aeroelastician who is not directed to other programs when minor changes have to be made for parametric studies. Also identification tags are generated which may be required by the interpolation of the elastomechanical data to the surface grid.

1420

Inspection

Attention has been paid to provide the user with 2-D and 3-D plot facilities to inspect all the data at the beginning, during and at the end of the simulation. Again this reduces the workload for the aeroelastician who is not directed to other programs for visualisation.

Grid generation

The grid generator provides a **OH** mono-block grid about the surface description of the complete aircraft with embedded upwind slits and downwind slits (wake surfaces). The grids have acceptable quality about concave areas such as airfoil noses and wing-fuselage junctions and are easy to be generated by 'non-grid expert' applicators. The consequence of some limitations in accuracy of the mono-block grid approach to more complex configurations is considered as more acceptable for aeroelastic applications than for performance design. The grid generation is performed by the hyperbolic grid generation method described in [10, 11] which introduces control terms derived from fluid analogies in concave areas where the standard hyperbolic grid generator fails. The effort to generate OH grids around transport type aircraft with mild concavities is low enough to be accepted by 'non-grid expert applicators'. The mapping from the computational space to the physical domain is based on the equations:

$$\frac{\vec{r}_\xi . \vec{r}_\zeta}{\mid r_\xi \mid\mid r_\zeta \mid} = \cos\varphi, \qquad (1)$$

$$\frac{\vec{r}_\eta . \vec{r}_\zeta}{\mid r_\eta \mid\mid r_\zeta \mid} = \cos\theta, \qquad (2)$$

$$\mid\vec{r}_\xi . (\vec{r}_\eta \times \vec{r}_\zeta)\mid = V. \qquad (3)$$

Here (ξ, η and ζ) denote the coordinates of the computational space, θ and ϕ are the angle control terms and V is the volume of the grid cells.

In the solution of the aforementioned equations additional dissipation terms are applied which are well described in [12]. In addition metric regularisation terms have been developed to guarantee a proper behavior at multi-valued axis, multi-valued slit tips, strongly swept surfaces and non-smooth surface grids at wing-body junctions, tip regions, etc.

With respect to the angle control terms the following options are provided:

1. They are supposed to be zero. In this case one relies on the dissipation terms for rendering concave domains.

2. The terms are evaluated by an aerodynamic panel method.

3. The terms are provided by the curvilinear surface spline method which is straightforwardly derived from the planar surface spline method[13]:

$$\cos\theta = a + b\xi + c\eta + \sum_{m=1}^{M} d_m r^2 \ln r^2 \qquad (4)$$

where $r^2 = (\xi - \xi_m)^2 + (\eta - \eta_m)^2$ and m denotes the points at plane boundaries and at strong concave and convex areas on which angles are prescibed. A similar formula is applied to $\cos\varphi$.

The prescribed angles and positions are automatically calculated for the few areas which experience strong concave or convex angles and equation (4) takes care of a smooth distribution even in very concave and convex corners where two positions on each leg of the corner are applied with opposite angles. The coefficients of the latter equation is solved by equating it for the M points together with the three constraints:

$$\sum_{m=1}^{M} d_m = 0,$$

$$\sum_{m=1}^{M} d_m \xi_m = 0,$$

and

$$\sum_{m=1}^{M} d_m \eta_m = 0.$$

In addition to the abovementioned formulations the computer program has been designed such that it is possible to start with an orthogonal grid. Post-elliptic smoothing with control functions [14] is embedded and an algebraic grid generation scheme method is applied as soon as the concave zones are largely resolved by the present method.

The method is later to be extented to a multi-sector method to aim at configurations for which the current method fails to produce grids of acceptable quality.

Aerodynamic models

At this time the most practical set of equations to model transonic flow about general aircraft configurations are no doubt the Thin Layer Navier Stokes equations followed by the Euler equations. From recent developments [15, 16] the conclusion might be drawn that the algorithms which apply subiterations within each time-step are the most efficient ones and very little room for improvement is left. However, the simulation

of unsteady flow about complete aircraft configurations by solving these equations is about one order slower as the solution by potential-based solvers on the same grid. In addition the grid should be about one order finer (3-D) to obtain reliable data. Yet, these methods are not suitable in routine simulations on the current generation of workstations.

When the unsteady aerodynamic flow is modeled in the time domain by the unsteady full potential equation and applied to flows with strong shock waves, results are obtained where shock waves are too strong and located too far aft on the airfoil in comparison with results obtained from Euler methods. This is mainly due to the neglect of entropy and vorticity. This modeling defect can be cured by means of the Clebsch potential [7]. By this shock-generated entropy as well as shock-generated vorticity are modeled such that flows with strong shock waves are treated in a non-approximate **exact** manner while retaining its cost efficiency in comparison with the aforementioned equations.

The modeling by the unsteady transonic small disturbance potential method is less appropriate due to the occurring oblique shock waves on swept parts of the configuration which cannot be resolved properly without additional changes [17].

The potential-based solvers should be completed by implementation of a correction for viscous effects to obtain a correct physical model.

The following sections present details of the full potential models which are currently applied and mention alternative models which are in the process of development.

Full potential model

The computational modeling for solving the unsteady full potential equation is guidelined by the method of Shankar [8] and is described below.

When applying the body-fitted coordinate system represented by $\tau = t, \xi = \xi(x,y,z,t), \eta = \eta(x,y,z,t)$ and $\zeta = \zeta(x,y,z,t)$ where $\zeta = 0$ denotes the surface of the body and slits, and introducing the disturbance potential ϕ the flow equations take the form:

Velocity $\vec{q} = \vec{q}_\infty + H^T \vec{\nabla}\phi$, where $\vec{\nabla} = (\frac{\partial\cdot}{\partial\xi}, \frac{\partial\cdot}{\partial\eta}, \frac{\partial\cdot}{\partial\zeta})^T$
and

$$H = \begin{pmatrix} \xi_x & \xi_y & \xi_z \\ \eta_x & \eta_y & \eta_z \\ \zeta_x & \zeta_y & \zeta_z \end{pmatrix}, \qquad (5)$$

where

$$\begin{aligned}
\xi_x &= (y_\eta z_\zeta - y_\zeta z_\eta)/j &, \\
\xi_y &= (z_\eta x_\zeta - z_\zeta x_\eta)/j &, \\
\xi_z &= (x_\eta y_\zeta - x_\zeta y_\eta)/j &, \\
\eta_x &= (y_\zeta z_\xi - y_\xi z_\zeta)/j &, \\
\eta_y &= (z_\zeta x_\xi - z_\xi x_\zeta)/j &, \quad (6) \\
\eta_z &= (x_\zeta y_\xi - x_\xi y_\zeta)/j &, \\
\zeta_x &= (y_\xi z_\eta - y_\eta z_\xi)/j &, \\
\zeta_y &= (z_\xi x_\eta - z_\eta x_\xi)/j &, \\
\zeta_z &= (x_\xi y_\eta - x_\eta y_\xi)/j &,
\end{aligned}$$

with

$$j = x_\xi(y_\eta z_\zeta - y_\zeta z_\eta) + y_\xi(z_\eta x_\zeta - z_\zeta x_\eta) + z_\xi(x_\eta y_\zeta - x_\zeta y_\eta). \tag{7}$$

Speed of sound

$$a^2 = \frac{1}{M_\infty^2} + \frac{\gamma-1}{2}(1 - \vec{q}\cdot\vec{q} - 2\phi_\tau - 2\vec{\sigma}_t\cdot\vec{\nabla}\phi)\}, \tag{8}$$

where

$$\vec{\sigma} = (\xi, \eta, \zeta)^T \text{ with } \vec{\sigma}_t = -H(x,y,z)_t^T. \tag{9}$$

Density

$$\rho = \{1 + \frac{\gamma-1}{2}M_\infty^2(1 - \vec{q}\cdot\vec{q} - 2\phi_\tau - 2\vec{\sigma}_t\cdot\vec{\nabla}\phi)\}^{\frac{1}{\gamma-1}}. \tag{10}$$

Pressure

$$C_p = \frac{2}{\gamma M_\infty^2}(\rho^\gamma - 1). \tag{11}$$

Conservation of mass

$$\left(\frac{\rho}{J}\right)_\tau + \vec{\nabla}\cdot\left(\frac{\rho\vec{Q}}{J}\right) = 0, \tag{12}$$

where

$$\vec{Q} = (U, V, W)^T = \vec{\sigma}_t + H\vec{q}. \tag{13}$$

Sonic mass flux

$$\rho^* q^* = \frac{1}{M_\infty}$$

$$\left(\frac{2 + (\gamma-1)M_\infty^2 - 2(\gamma-1)M_\infty^2(\phi_\tau + \vec{\sigma}_t\cdot\vec{\nabla}\phi)}{\gamma+1}\right)^{\frac{1}{\gamma-1}+\frac{1}{2}} \tag{14}$$

Also $a = q^*$.

Mass flux equation

$$\left(\frac{\rho}{J}\right)_\tau + \vec{\nabla}\cdot\left(\frac{\overleftarrow{\rho}\vec{Q}}{J}\right) = 0. \tag{15}$$

The upwind density $\overleftarrow{\rho}$ is defined as:

$$\overleftarrow{\rho} = \rho - \frac{(\vec{Q} \cdot \overleftarrow{\Delta \nabla})(\rho q)^-}{|Q| q}, \qquad (16)$$

where

$$\overleftarrow{\Delta \nabla} = (\Delta \xi \overleftarrow{\frac{\partial}{\partial \xi}}, \Delta \eta \overleftarrow{\frac{\partial}{\partial \eta}}, \Delta \zeta \overleftarrow{\frac{\partial}{\partial \zeta}})^T, \qquad (17)$$

and

$$\begin{array}{llll} (\rho q)^- & = & \rho q - \rho^* q^* & M > 1 \\ (\rho q)^- & = & 0 & M \le 1 \end{array}, \qquad (18)$$

while $M = \frac{q}{a}$ and $\overleftarrow{\#}$ denotes upwind differentiation with respect to the direction of the fluid velocity.

Freestream consistency When no disturbances occur in the flow ($\phi = 0$) the equation (15) is in general not satisfied due to the formulation in curvilinear coordinates and the applied discretisation.

To account for this offset the right-hand side of equation (15) is modified to:

$$f = \left(\frac{\rho_\infty}{J}\right)_\tau + \vec{\nabla} \cdot \left(\frac{\rho_\infty \vec{Q}_\infty}{J}\right), \qquad (19)$$

where

$$\vec{Q}_\infty = \vec{\sigma}_t + H \vec{q}_\infty. \qquad (20)$$

Wake boundary conditions and Kutta condition
Through the wake and at the trailing edge the pressure is supposed to be continuous:

$$\llbracket C_p \rrbracket = 0, \qquad (21)$$

or

$$\llbracket \rho \rrbracket = 0, \qquad (22)$$

or

$$\llbracket \vec{q} \cdot \vec{q} + 2\phi_\tau + 2\vec{\sigma}_t \cdot \vec{\nabla}\phi \rrbracket = 0. \qquad (23)$$

Also the mass flux is continuous:

$$\llbracket \rho W \rrbracket = 0. \qquad (24)$$

The brackets $\llbracket$ and $\rrbracket$ define the difference of the bracketed quantity through the wake slit. The wake geometry is supposed to be explicitly described.

Boundary conditions at the body At the body zero penetration is imposed:

$$\vec{q} \cdot \vec{N}_b = \vec{r}_t \cdot \vec{N}_b, \qquad (25)$$

where $\vec{N}_b = \frac{(\zeta_x, \zeta_y, \zeta_z)^T}{\sqrt{\zeta_x^2 + \zeta_y^2 + \zeta_z^2}}$ denotes the normal at the body and $\vec{r}_t = (x, y, z)_t^T = \vec{q}_b$ is the velocity of the body. Applying:

$$\vec{\sigma}_t = -H(x, y, z)_t^T, \qquad (26)$$

the equation simplifies to:

$$W = 0. \qquad (27)$$

Transpiring boundary conditions at the body
When the body-fitted coordinates do not follow the motion of the body approximate boundary conditions are applied:

$$\vec{q} \cdot \vec{N}_b = \vec{h}_{b_t} \cdot \vec{N}_b + (\vec{h}_{b_t} - \vec{q}) \cdot \vec{n}_b, \qquad (28)$$

where

$$\vec{n}_b = \frac{\vec{n}^* - (\vec{n}^* \cdot \vec{N}_b)\vec{N}_b}{\sqrt{(\zeta_x^2 + \zeta_y^2 + \zeta_z^2)}}, \qquad (29)$$

with

$$\vec{n}^* = \vec{r}_\xi \times \vec{h}_{b_\eta} - \vec{r}_\eta \times \vec{h}_{b_\xi}, \qquad (30)$$

or

$$\frac{W}{\sqrt{\zeta_x^2 + \zeta_y^2 + \zeta_z^2}} = \vec{h}_{b_t} \cdot \vec{N}_b + (\vec{h}_{b_t} - \vec{q}) \cdot \vec{n}_b. \qquad (31)$$

h_b denotes the displacement of the body which is not dealt with in the coordinate system. In case the normalisation with respect to the normals $\vec{N}_b$ and $\vec{n}_b$ is not made the equation simplifies to:

$$W = \vec{h}_{b_t} \cdot \vec{N}_b^\star + (\vec{h}_{b_t} - \vec{q}) \cdot \vec{n}_b^\star, \qquad (32)$$

where $\vec{N}_b^\star = (\zeta_x, \zeta_y, \zeta_z)^T$ and

$$\vec{n}_b^\star = \vec{n}_b \sqrt{\zeta_x^2 + \zeta_y^2 + \zeta_z^2}.$$

Boundary conditions at the far field In the far field absorbing boundary conditions [18] are applied:

$$\frac{M_\infty}{\sqrt{1 - M_\infty^2}} \left(1 - \frac{M_\infty}{\sqrt{1 - M_\infty^2}} \frac{x}{R}\right) \left(\phi_\tau + \vec{\sigma}_t \cdot \vec{\nabla}\phi\right) + \left(\frac{\vec{r} \cdot H^T \vec{\nabla}\phi}{R}\right) + \frac{\phi}{R} = 0. \qquad (33)$$

$R = \sqrt{\frac{x^2}{1 - M_\infty^2} + y^2 + z^2}$ denotes the compressible distance to the center of gravity of the body.

Time integration

A first-order time accurate integration is applied to the equation in the field and at the boundaries:

Conservation of mass

$$\frac{(j\rho)^{n+1} - (j\rho)^n}{\triangle\tau} + \vec{\nabla}\cdot\left(j\overleftarrow{\rho}\vec{Q}\right)^{n+1} = f^{n+1}. \quad (34)$$

n denotes the solution at the time interval τ^n and the time step $\triangle\tau = \tau^{n+1} - \tau^n$. Furthermore:

$$\rho^{\gamma-1^n} = a^{2^n}, \quad (35)$$

with

$$a^{2^n} = 1 - \frac{\gamma-1}{2}(\vec{q}^n\cdot\vec{q}^n + 2\frac{\phi^n - \phi^{n-1}}{\triangle\tau} + 2\vec{\sigma}_t\cdot\vec{\nabla}\phi^n), \quad (36)$$

and

$$\rho^{\gamma-1^{n+1}} = a^{2^{n+1}}, \quad (37)$$

with

$$a^{2^{n+1}} = 1 -$$
$$\frac{\gamma-1}{2}(\vec{q}^{n+1}\cdot\vec{q}^{n+1} + 2\frac{\phi^{n+1} - \phi^n}{\triangle\tau} + 2\vec{\sigma}_t\cdot\vec{\nabla}\phi^{n+1}). \quad (38)$$

At the wake the mass equation at the upper and lower side is combined to one equation.

Wake boundary conditions and Kutta condition

$$\llbracket (\vec{q}\cdot\vec{q})^{n+1} + 2\frac{(\phi^{n+1} - \phi^n)}{\triangle\tau} + 2\vec{\sigma}_t\cdot\vec{\nabla}\phi^{n+1}\rrbracket = 0. \quad (39)$$

Boundary conditions at the body

$$W^{n+1} = 0. \quad (40)$$

Transpiring boundary conditions at the body

$$W^{n+1} = \vec{h}_{b_t}\cdot\vec{N}_b^{\star} + (\vec{h}_{b_t} - \vec{q}^{n+1})\cdot\vec{n}_b^{\star}. \quad (41)$$

Absorbing conditions at the far field

$$\left(\frac{(\phi^{n+1} - \phi^n)}{\triangle\tau} + \vec{\sigma}_t\cdot\vec{\nabla}\phi^{n+1}\right)$$
$$+ \left(\frac{\vec{r}\cdot H^T\vec{\nabla}\phi^{n+1}}{r}\right) + \frac{\phi^{n+1}}{r} = 0. \quad (42)$$

Newton procedure

The solution of the aforementioned equations at $n + 1$ is obtained by means of the well-known Newton (subiteration) procedure [8]. Assuming that a guess to the solution at $n + 1$ is available (denoted by $\phi^{\heartsuit}$), the solution is improved by the process given below. This process is repeated as many times as required for accuracy. The number of subiterations depends on the time step. Usually 2 iterations are sufficient when about 128 time steps are used for a complete period. About O(10) subiterations are required when a period is modeled by 16 time steps.

The process is described by:

Conservation of mass

$$L_m(\phi^{n+1}-\phi^{\heartsuit}) = \frac{(j\rho)^{\heartsuit} - (j\rho)^n}{\triangle\tau} + \vec{\nabla}\cdot\left(j\overleftarrow{\rho}\vec{Q}\right)^{\heartsuit} - f^{\heartsuit}. \quad (43)$$

The Jacobian of equation (34) is approximated as:

$$L_m = \frac{j^{\heartsuit}\rho^{\heartsuit}}{\triangle\tau a^{2^{\heartsuit}}}\left(\frac{1}{\triangle\tau} + \vec{Q}^{\heartsuit}\cdot\overleftarrow{\vec{\nabla}}_Q\right)$$
$$+ \overleftarrow{\vec{\nabla}}\cdot\left\{j^{\heartsuit}\overleftarrow{\rho}^{\heartsuit}\left[-HH^T\vec{\nabla} + \frac{\vec{Q}^{\heartsuit}}{a^{2^{\heartsuit}}}\left(\frac{1}{\triangle\tau} + \vec{Q}^{\heartsuit}\cdot\vec{\nabla}\right)\right]\right\}, \quad (44)$$

where

$$\overleftarrow{\vec{\nabla}} = \vec{\nabla} \quad | M \leq 1$$
$$\overleftarrow{\vec{\nabla}} = \overleftarrow{\nabla} \quad | M > 1 \quad \text{upwind gradient,} \quad (45)$$

and

$$\overleftarrow{\vec{\nabla}}_Q = \vec{\nabla} \quad | Q \leq 0 ,$$
$$\overleftarrow{\vec{\nabla}}_Q = \overleftarrow{\nabla} \quad | Q > 0 . \quad (46)$$

At the wake the mass equation at the upper and lower side is combined to one equation which results in the Jacobian:

$$L_{mw} = L_m^{upper} + L_m^{lower}. \quad (47)$$

Wake boundary conditions and Kutta condition

$$L_w(\phi^{n+1} - \phi^{\heartsuit}) = -\llbracket \vec{q}^{\heartsuit}\cdot\vec{q}^{\heartsuit} + 2\frac{(\phi^{\heartsuit} - \phi^n)}{\triangle\tau}$$
$$+ 2\vec{\sigma}_t\cdot\vec{\nabla}\phi^{\heartsuit}\rrbracket, \quad (48)$$

where

$$L_w = \llbracket 2\vec{Q}^{\heartsuit}\cdot\overleftarrow{\vec{\nabla}}_Q + \frac{2}{\triangle\tau}\rrbracket . \quad (49)$$

Boundary conditions at the body

$$L_b(\phi^{n+1} - \phi^\heartsuit) = W^{n+1} = 0, \qquad (50)$$

where

$$L_b = -(g_{13}, g_{23}, g_{33})^T \cdot \vec{\nabla}. \qquad (51)$$

The body boundary equation is implicitly applied by substituting the expression $W^{n+1} = 0$ in the mass equation at the surface. The additional linearization step is not necessary, however, it can be embedded [8] in the mass equation to improve on the stability of the approximate factorisation method.

Transpiring boundary conditions at the body

$$L_b(\phi^{n+1} - \phi^\heartsuit) = W^{n+1} - \vec{h}_{b_t} \cdot \vec{N}_b^\star - (\vec{h}_{b_t} - \vec{q}^\heartsuit) \cdot \vec{n}_b^\star, \qquad (52)$$

where

$$L_b = -(g_{13}, g_{23}, g_{33})^T \cdot \vec{\nabla}. \qquad (53)$$

The body boundary equation is implicitly applied by substituting the expression $W^{n+1} - \vec{h}_{b_t} \cdot \vec{N}_b^\star - (\vec{h}_{b_t} - \vec{q}^{n+1}) \cdot \vec{n}_b^\star$ in the mass equation at the surface.

Absorbing conditions at the far field

$$L_a(\phi^{n+1} - \phi^\heartsuit) = \left(\frac{(\phi^\heartsuit - \phi^n)}{\Delta\tau} + \vec{\sigma}_t \cdot \vec{\nabla}\phi^\heartsuit \right)$$
$$+ \left(\frac{\vec{r} \cdot H^T \vec{\nabla}\phi^\heartsuit}{r} \right) + \frac{\phi^\heartsuit}{r}, \qquad (54)$$

where

$$L_a = -\frac{1}{\Delta\tau} - \vec{\sigma}_t \cdot \vec{\nabla} - \left(\frac{\vec{r} \cdot H^T \vec{\nabla}}{r} \right) - \frac{1}{r}. \qquad (55)$$

In the aforementioned equations L denotes the Jacobian of the nonlinear system and the superscript $\heartsuit$ denotes the intermediate solution. At convergence $\phi^\heartsuit \Rightarrow \phi^{n+1}$. The Newton iteration procedure is applied utilizing a consistent guess of the density and the potential at the start. A proper guess has to be made for $\phi^\heartsuit$ and, more importantly, for a consistent $\rho^\heartsuit$ when the Newton procedure starts. The obvious choice $\phi^\heartsuit = \phi^n$ and $\rho^\heartsuit = \rho^n$ is **inconsistent** with the applied Jacobian! In that case one should be aware that the most recent potential time derivative $\phi_\tau = \frac{\phi^\heartsuit - \phi^n}{\Delta\tau}$ should be put to **zero** (neutralized) at the start of the process in all variables and equations that employ it at the state $\heartsuit$ to achieve consistency.

This is most easily demonstrated for the simple case of the following equation:

$$g = \phi_{tt} = 0.$$

Applying time linearization:

$$\phi^{n+1} - \phi^\heartsuit = -g^{\heartsuit,n,n-1} = -(\phi^\heartsuit - \phi^n) + (\phi^n - \phi^{n-1}).$$

Next, choosing $\phi^\heartsuit = \phi^n$, the correct equation to be solved becomes:

$$\phi^{n+1} - \phi^n = -g^{n,n,n-1} = -\underline{0} + (\phi^n - \phi^{n-1}),$$

wheras the inconsistent one:

$$\phi^{n+1} - \phi^n = -(\phi^n - \phi^{n-1}) + (\phi^n - \phi^{n-1}) = 0,$$

demonstrates what happens when ϕ_τ is extrapolated from the previous time-step.

The neutralisation is easily accomplished for the wake and far field boundary equations. With respect to the mass flux and to avoid the recalculation of nonlinear terms, it is advisable to **subtract** the time derivatives by linearization. In the literature a lot of attention is given to the generation of a proper guess using a so-called time linearization concept, because of often encountered failures of the method using other (inconsistent) guesses.

Also this seems to be a reason for resorts frequently made to higher-order time integration which is less critical with respect to the starting procedure. Proper guesses are depicted in table (1) below.

N.	$\phi^\heartsuit$	$\rho^\heartsuit$
1	ϕ^n	$\rho^n(1 + \frac{\phi^n - \phi^{n-1}}{a^{2^n}\Delta\tau})$ **note the sign!**
2	$2\phi^n - \phi^{n-1}$	$\rho^n(1 - \frac{1}{a^{2^n}}(\vec{Q}^n \cdot \overleftarrow{\nabla} + \frac{1}{\Delta\tau}))(\phi^n - \phi^{n-1}))$

Table 1: Options for starting Newton procedure

In deriving the aforementioned Jacobians the linearization of the speed of sound and density is applied:

$$a^2 = a^{2^n} - (\gamma - 1)\left(\vec{Q} \cdot \vec{\nabla} + \frac{\partial}{\partial\tau} \right)(\phi - \phi^n), \qquad (56)$$

and

$$\rho = \rho^n - \frac{\rho^n}{a^{2^n}}\left(\vec{Q} \cdot \vec{\nabla} + \frac{\partial}{\partial\tau} \right)(\phi - \phi^n). \qquad (57)$$

Approximate factorisation

The Jacobian system matrix ($L = L_m, L_{mw}, L_w$ and L_a) is inverted by approximate factorisation:

$$L(\phi^{n+1} - \phi^{\triangledown}) \simeq L_\xi L_\eta L_\zeta (\phi^{n+1} - \phi^{\triangledown}) \simeq Res^{\triangledown,n,n-1},$$
(58)

with Res the residual of the equations. In the flow the Res and the operators are scaled with $\frac{\rho^{\triangledown} j^{\triangledown}}{(\Delta\tau)^2 a^{2\triangledown}}$ and have the form:

$$L_\xi = 1 + 2\Delta\tau U \overleftarrow{\frac{\partial}{\partial\xi}}_U$$
$$+ \frac{(\Delta\tau)^2 a^{2\triangledown}}{j^{\triangledown} \rho^{\triangledown}} \overleftarrow{\frac{\partial}{\partial\xi}} \left[j^{\triangledown} \overleftarrow{\rho^{\triangledown}} \left(\frac{U^{2\triangledown}}{a^{2\triangledown}} - g_{11} \right) \frac{\partial}{\partial\xi} \right], \quad (59)$$

$$L_\eta = 1 + 2\Delta\tau V \overleftarrow{\frac{\partial}{\partial\eta}}_V$$
$$+ \frac{(\Delta\tau)^2 a^{2\triangledown}}{j^{\triangledown} \rho^{\triangledown}} \frac{\partial}{\partial\eta} \left[j^{\triangledown} \overleftarrow{\rho^{\triangledown}} \left(\frac{V^{2\triangledown}}{a^{2\triangledown}} - g_{22} \right) \frac{\partial}{\partial\eta} \right], \quad (60)$$

$$L_\zeta = 1 + 2\Delta\tau W \overleftarrow{\frac{\partial}{\partial\zeta}}_W$$
$$+ \frac{(\Delta\tau)^2 a^{2\triangledown}}{j^{\triangledown} \rho^{\triangledown}} \frac{\partial}{\partial\zeta} \left[j^{\triangledown} \overleftarrow{\rho^{\triangledown}} \left(\frac{W^{2\triangledown}}{a^{2\triangledown}} - g_{33} \right) \frac{\partial}{\partial\zeta} \right]. \quad (61)$$

In these equations upwinding is applied to the second term with respect to the contravariant velocity and also it should be noted that upwinding is applied in the L_ξ operator for improving stability in supersonic areas which renders the bandwidth to 4. The wake and Kutta equations are implicitly coupled in the L_ζ operator.

Discretisation

The discretisation method is related to the finite volume method described for steady flow in [19]. This method minimizes the number of density evaluations with a factor of 4. The odd-even decoupling introduced by this scheme is prevented by a lumping operator which is related to the Jacobian system matrix and guarantees a solid performance of the approximate factorisation method. The lumping operator is added to the RHS of equation (58):

$$L(\phi^{n+1} - \phi^{\triangledown}) \simeq L_\xi L_\eta L_\zeta (\phi^{n+1} - \phi^{\triangledown}) \simeq Res^{\triangledown,n,n-1}$$
$$+ \kappa((L_\xi + L_\eta + L_\zeta) - (V_\xi + V_\eta + V_\zeta))(\phi^n - \phi^{\triangledown}), \quad (62)$$

where κ is the lumping factor($0 < \kappa < 1$), V_ξ, V_η, and V_ζ denote the approximate Jacobian operator of the applied volume discretisation and the approximate factorisation operators L_ξ, L_η, and L_ζ are obtained by lumping of V in ξ, η, and ζ direction, respectively.

Vorticity and entropy corrections

This section presents the changes which apply to the full potential model when strong shock waves occur by introducing the Clebsch potential Υ which has the following consequences:

Velocity $\vec{q} = \vec{q}_\infty + H^T \vec{\nabla}\phi + \Delta S H^T \vec{\nabla}\Upsilon$.

Speed of sound

$$a^2 = \frac{1}{M_\infty^2} + \frac{\gamma - 1}{2} ($$
$$1 - \vec{q}\cdot\vec{q} - 2\phi_\tau - 2\vec{\sigma}_t \cdot \vec{\nabla}\phi - 2\Delta S \Upsilon_\tau - 2\Delta S \vec{\sigma}_t \cdot \vec{\nabla}\Upsilon). \quad (63)$$

Density

$$\rho = e^{-\frac{\Delta S}{R}} \{1 + \frac{\gamma - 1}{2} M_\infty^2 ($$
$$1 - \vec{q}\cdot\vec{q} - 2\phi_\tau - 2\vec{\sigma}_t \cdot \vec{\nabla}\phi - 2\Delta S \Upsilon_\tau - 2\Delta S \vec{\sigma}_t \cdot \vec{\nabla}\Upsilon)\}^{\frac{1}{\gamma-1}}. \quad (64)$$

Pressure

$$C_p = \frac{p - p_\infty}{\frac{1}{2}\rho_\infty q_\infty^2} = \frac{2}{\gamma M_\infty^2} (e^{(\gamma-1)\frac{\Delta S}{R}} \rho^\gamma - 1). \quad (65)$$

Entropy equation

$$\frac{D(\Delta S)}{DT} = 0, \quad (66)$$

with $\frac{D\#}{DT} = \frac{\partial\#}{\partial\tau} + (\vec{Q} \cdot \vec{\nabla})\#$.

Entropy rise The entropy rise is generated at shock waves according to:

$$\frac{\Delta S}{R} = \frac{1}{\gamma - 1} ln \left(\frac{\left(1 + \frac{2\gamma}{\gamma+1}(M_s^2 - 1)\right)}{\left(\frac{(\gamma+1)M_s^2}{(\gamma-1)M_s^2+2}\right)^\gamma} \right), \quad (67)$$

where M_s denotes the Mach number normal to the shock:

$$M_s = \frac{\vec{q}\cdot\vec{n}_s - U_s}{a}. \quad (68)$$

U_s denotes the shock speed in normal direction:

$$U_s = \frac{[\![\rho\vec{q}\cdot\vec{n}_s]\!]}{[\![\rho]\!]} \quad (69)$$

and the normal to the shock follows from equating the tangential velocities across the shock surface:

$$\vec{n}_s = \frac{[\![\vec{q}]\!]}{|[\![\vec{q}]\!]|}. \quad (70)$$

Clebsch potential equation

$$\frac{D\Upsilon}{DT} = -\frac{a^2}{\gamma R}. \quad (71)$$

Sonic mass flux The sonic mass flux is:

$$\rho^* q^* = \frac{e^{-\frac{\Delta S}{R}}}{M_\infty(\gamma+1)^{\frac{1}{\gamma-1}+\frac{1}{2}}}(\#)^{\frac{1}{\gamma-1}+\frac{1}{2}}, \qquad (72)$$

with

$$\# = 2 + (\gamma-1)M_\infty^2$$

$$-2(\gamma-1)M_\infty^2(\phi_\tau + \Delta S\Upsilon_\tau + \vec{\sigma}_t\cdot\vec{\nabla}\phi + \Delta S\vec{\sigma}_t\cdot\vec{\nabla}\Upsilon). \qquad (73)$$

Wake boundary conditions and Kutta condition
Through the wake and at the trailing edge the pressure is supposed to be continuous:

$$⫽ C_p ⫽ = 0. \qquad (74)$$

It should be noted that the density and the speed of sound are **not** continuous through the wake:

$$⫽ \rho ⫽ \neq 0, \qquad (75)$$

and

$$⫽ a^2 ⫽ = ⫽ \vec{q}\cdot\vec{q} + 2\phi_\tau + 2\vec{\sigma}_t\cdot\vec{\nabla}\phi$$

$$+ 2\Delta S\Upsilon_\tau + 2\Delta S\vec{\sigma}_t\cdot\vec{\nabla}\Upsilon ⫽ \neq 0. \qquad (76)$$

Only the mass flux is required to be continuous:

$$⫽ \rho\vec{q}\cdot\vec{N}_w ⫽ = 0. \qquad (77)$$

The other equations (12-18) only change by simply fill in the aforementioned quantities. The embedding of these corrections in the computational model is described in [7].

Time-linearized full potential model

Hounjet's diverging rate approach introduced in [4] and applied in [5, 6] offers the possibility for any method to obtain generalized forces very efficiently. This approach is based on the following steps:

1. Obtain aerodynamic data for a purely exponentially diverging motion with the time function e^{st} where s is positive and real.

2. Make a polynomial fit through those data.

3. Suppose the fit (which is the transfer function) to be valid throughout the complex s plane, including imaginary s which represents harmonic motions.

The first step involves limited changes to be made only with respect to the residual part of the equations and the full reuse of the linear system. The time step should be interpreted as the diverging rate. The linear system can be solved with the AF scheme which involves O(10) iterations. It is foreseen to apply other sparse matrix solvers. About 10 diverging rates are necessary to cover the complete frequency range for one vibration mode. The conclusion might be drawn that the cost is equivalent to the cost of **one** steady application per mode which is very advantageous. By convolution the transfer function is defined and direct simulation can be performed.

Panel Methods

The linear panel methods should be applied for about O(10) diverging rates. Thereafter a Padé fit is made, the transfer function is defined and direct simulation can be performed.

Viscous Methods

Viscous effects will be modeled by an integral boundary layer method. It is expected that this extention will improve the prediction of shock position and control surface loads, and will enable the prediction of aeroelastic characteristics naer the buffet boundary.

Thin Layer NS code

Work has been started on a Thin Layer NS code which is planned to be integrated in the system [20]. This adaption of the simulation method makes it applicable to fighter type configurations in vortex flow.

Simulations

The method enables the following types of simulation around 2-D and 3-D configurations:

1. Steady aerodynamic simulation at given M_∞ and angle of attack for rigid configuration;

2. Steady aeroelastic simulation with static deformations at given M_∞, angle of attack and dynamic pressure;

3. Unsteady aerodynamic simulation for forced motion or deformation at given M_∞, angle of attack, vibration mode and type of the motion (sinusoidal, impulse, jump, polynomial, etc.);

4. Unsteady aeroelastic simulation due to elastome-chanical motion or deformation at given M_∞, angle of attack, dynamic pressure and vibration modes.

Simulations can be performed about symmetric configurations with symmetric and/or anti-symmetric vibration modes with respect to the xy and xz planes. Also simulations are possible for wing-tail configurations and for complete bodies which require circumferential periodicity conditions to be applied.

Elastomechanical model

The elastomechanical model is split into a static part and a dynamic part which are explained in the following sections.

A(ero)E(lasto) Transfer

Because the models are based on different grids interpolation procedures are developed which transfer aerodynamic and elastomechanical data between the elastomechanical and aerodynamic surface grids. Also bounding boxes might be specified by the user for each vibration mode to ease the implementation of control surface effects, etc. Outside these boxes zero padding of the data is applied.

The following models are available to represent the elastomechanical data adequately on the aerodynamic surfaces and vice versa:

1. The well-known planar surface spline interpolation of [13]. In order to apply it to non-planar configurations the elastomechanic grid is simplified into planar surface grids and the connection to the aerodynamic surface grid is done on the basis of the nearest planar surface.

2. Straightforward extension of the planar surface spline interpolation of [13] in curvilinear coordinates. In this option the elastomechanic grid is projected on the aerodynamic surface grid. This is easily accomplished due to the fact that only one aerodynamic surface grid is involved. Note that the structural nodes in the configuration should be projected twice to the aerodynamic surface grid. The expression of the spline is given by equation (4).

3. Least Squares Polynomial approximation of the data. In this option the data is approximated by:

$$h = \sum_{i=0}^{L} \sum_{j=0}^{M} \sum_{k=0}^{N} a_{ijk} x^i y^j z^k. \qquad (78)$$

This option is very useful for smooth data, as encountered in dynamic stability applications.

4. Straightforward extension of the surface spline interpolation to volume spline interpolation. In this option the data which is supposed to approximately satisfy the 3-D bi-harmonic equation is interpolated by:

$$h = a + bx + cy + dz + \sum_{m=1}^{M} e_s r, \qquad (79)$$

where

$$r = \sqrt{(x - x_s)^2 + (y - y_s)^2 + (z - z_s)^2},$$

and m denotes the points on the structural grid. The coefficients of the latter equation are solved by equating them for the M points together with the four constraints:

$$\sum_{m=1}^{M} e_s = 0,$$

$$\sum_{m=1}^{M} e_s x_s = 0,$$

$$\sum_{m=1}^{M} e_s y_s = 0,$$

and

$$\sum_{m=1}^{M} e_s z_s = 0.$$

The volume spline method is the most promising one because it does not require any user interaction and can be applied to non-smooth data.

In general it is assumed that the elastomechanic data are obtained through NASTRAN so that for this case an interface is created.

Static elastomechanical model

The static deformation of the aircraft configuration is obtained by means of the 'free-free' flexibility matrix.

Dynamic elastomechanical model

The dynamic structural behavior of the aircraft is based on the generalized modal deflection approach. The dynamic deformations are expressed in generalized coordinates q_i and their associated modal mass M, damping D, stiffness K and vibration modes $\bar{h}_i$ which satisfy the equation:

$$M\ddot{q} + D\dot{q} + Kq = F \qquad (80)$$

where

$$F = \frac{\rho_\infty V_\infty^2}{2} \int_s C_p \vec{h}_i \cdot \vec{N} ds \qquad (81)$$

Equation (80) is transformed to first order:

$$d\dot{Q} + kQ = f \qquad (82)$$

where $Q = \begin{pmatrix} q \\ \dot{q} \end{pmatrix}, f = \begin{pmatrix} 0 \\ F \end{pmatrix}, d = \begin{pmatrix} 1 & 0 \\ 0 & M \end{pmatrix},$
and

$$k = \begin{pmatrix} 0 & -1 \\ K & D \end{pmatrix}.$$

$$\dot{Q} + d^{-1}kQ = d^{-1}f. \qquad (83)$$

The latter is solved by the well-known Newmark scheme:

$$Q^{n+1} - Q^n + \frac{\Delta\tau}{2}d^{-1}k(Q^{n+1} + Q^n) = \frac{\Delta\tau}{2}d^{-1}(f^{\heartsuit} + f^n). \qquad (84)$$

$$Q^{n+1} = \frac{\Delta\tau}{2}c^{-1}d^{-1}(f^{\heartsuit} + f^n) + c^{-1}(2I - c)Q^n, \qquad (85)$$

where:

$$c = I + \frac{\Delta\tau}{2}d^{-1}k. \qquad (86)$$

At the beginning of the Newton process the assumption is made:

$$f^{\heartsuit} = 2f^n - f^{n-1}.$$

Monitoring and Postprocessing

Direct monitoring and analysis of all aeroelastic quantities of interest are of major importance for the user. The analysis in the time domain is performed by means of exponential sine fitting using the well known Prony's method for obtaining initial guesses. Also an interface will be created to apply easily the analysing tools of LMS (Leuven Measurements Systems).

Others

Besides the vibration modes, two different sets of geometric disturbance fields may be applied by the user which are interpolated by the volume spline or polynomial spline method in bounding boxes specified by the user:

control modes With these modes it is possible to simulate the effect of inflow, a boundary layer, design changes, etc. These modes contribute to the transpiration boundary condition (28).
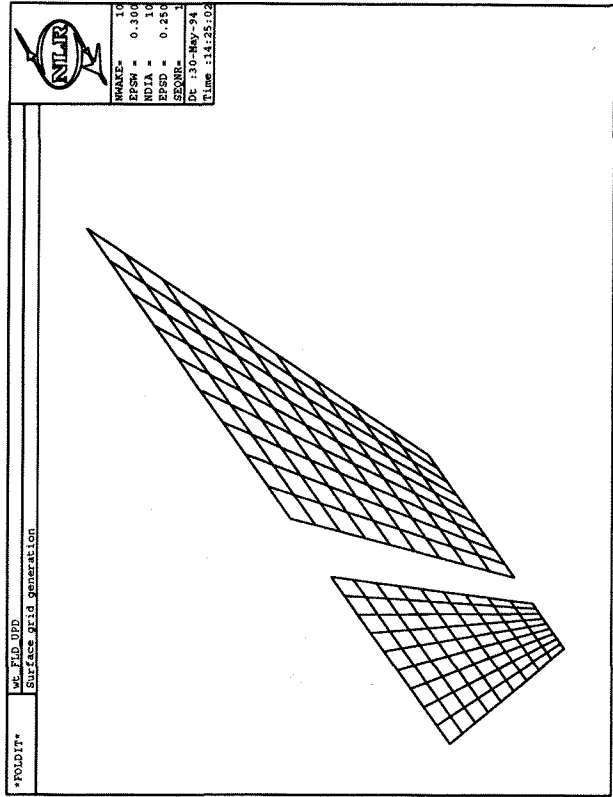

Figure 2: Surface grid of AGARD wing tail

pseudo vibration modes These modes allow for the calculation of forces on parts of the configuration using (81) and have no impact on the solution.

In order to facilitate the comparison with other reference pressure data during the simulation, the volume spline method is also used to interpolate arbitrary data to the aerodynamic surface grid.

Examples

The applicability range of the method is directed to 2-D airfoils, 3-D wings, 3-D wing-bodies, T-tails, etc. In this paper some applications of the method will be presented, which were not shown already in [7] and involved applications with and without the Clebsch potential to 2-D airfoils and 3-D wings. The examples here will focus on aeroelastic applications in 3-D and demonstrate the status of the aeroelastic environment.

Wing-tail model

In order to demonstrate the ability of the system to deal with multi-surfaces the unsteady AGARD planar
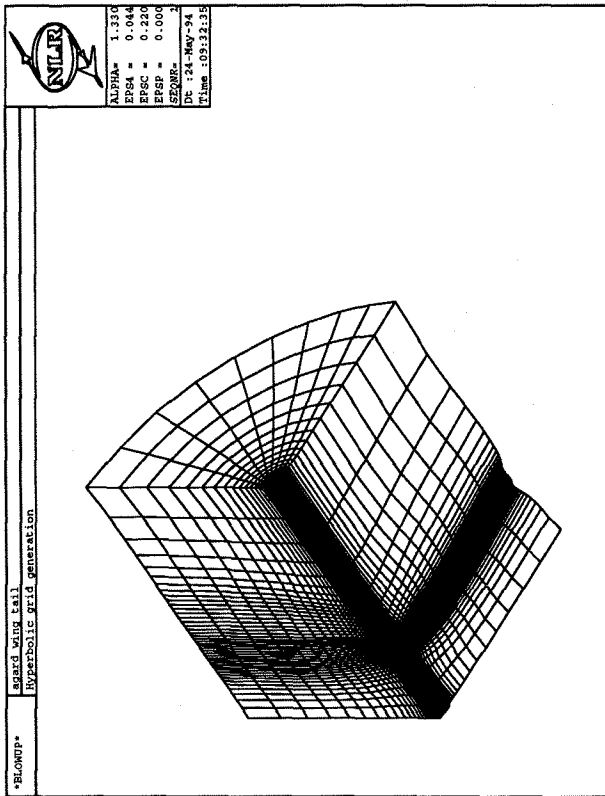
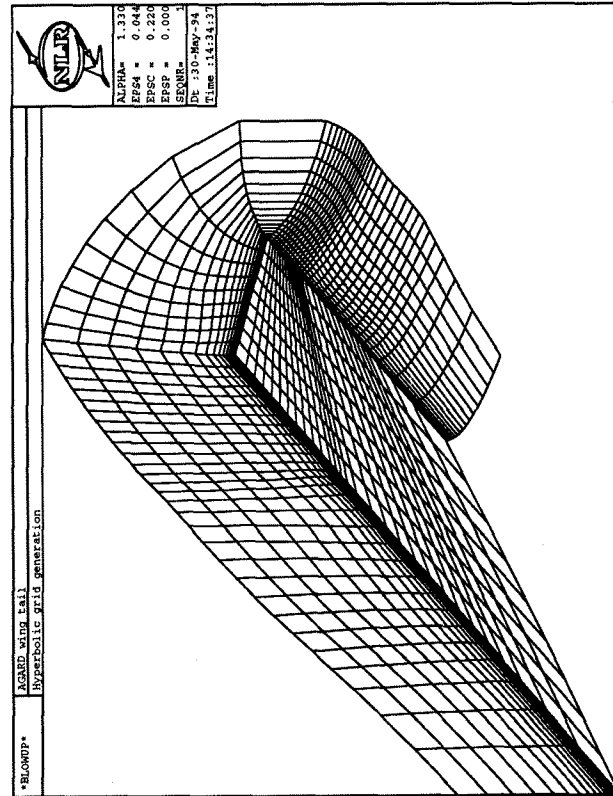Figure 3: Grid around AGARD wing tail

Figure 4: Grid around AGARD wing tail (close up)

wing-tail configuration with the tail in the plane of the wing has been considered.

The grid is depicted in figures 2-4 and shows the abillity of the grid generator to deal with strongly swept wings and non-uniform distributions. Also the double valued tip-axis is clearly visible. It should be noted that the coarse distributions on the surfaces are chosen in a way which is acceptable for lifting surface methods. Only 43x20x27 nodes are applied with 10x10 nodes on each side of the surfaces!

Unsteady calculations have been performed at $M_\infty = 0.8$ and k=0.5 in wing twisting.

By a parametric study with respect to the time step and the far field boundaries it was concluded that the application of 256 time steps with 2 subiterations during 3 periods on the current grid results in a 3 digit accuracy.

The geometry of the wing and tail consists of planar quadrilaterals with the following corner co-ordinates:

wing vertex	x	y	z	tail vertex	x	y	z
1	0	0	0	1	2.70	0	0
2	2.25	0	0	2	4.00	0	0
3	2.75	1	0	3	3.90	1	0
4	3.70	1	0	4	4.25	1	0

The symmetric displacement modes of the configuration are defined as follows:

no	wing h_z	tail h_z	mode
1	$\mid y \mid (x - 2.25 \mid y \mid -0.85)$	0	wing twisting
2	y^2	0	wing bending
3	0	$\mid y \mid$	tail 'rolling'
4	0	$(x - 3.35)$	tail pitching

Figure 5 shows the first harmonic pressure distributions as obtained with the present method and by the GUL method on the wing and the tail.

The following can be remarked:

- The leading edge of the tail experiences a large pressure difference with respect to the real part at the tip.

- The real part of the AESIM data is in good agreement with the GUL data at both the wing and the tail.

- The imaginary part of the AESIM data is in good agreement on the tail and a large part of the wing. At the tip the relatively small (Note the difference in scale between the real and imaginary figure) imaginary part on the wing is underpredicted by the AESIM method.
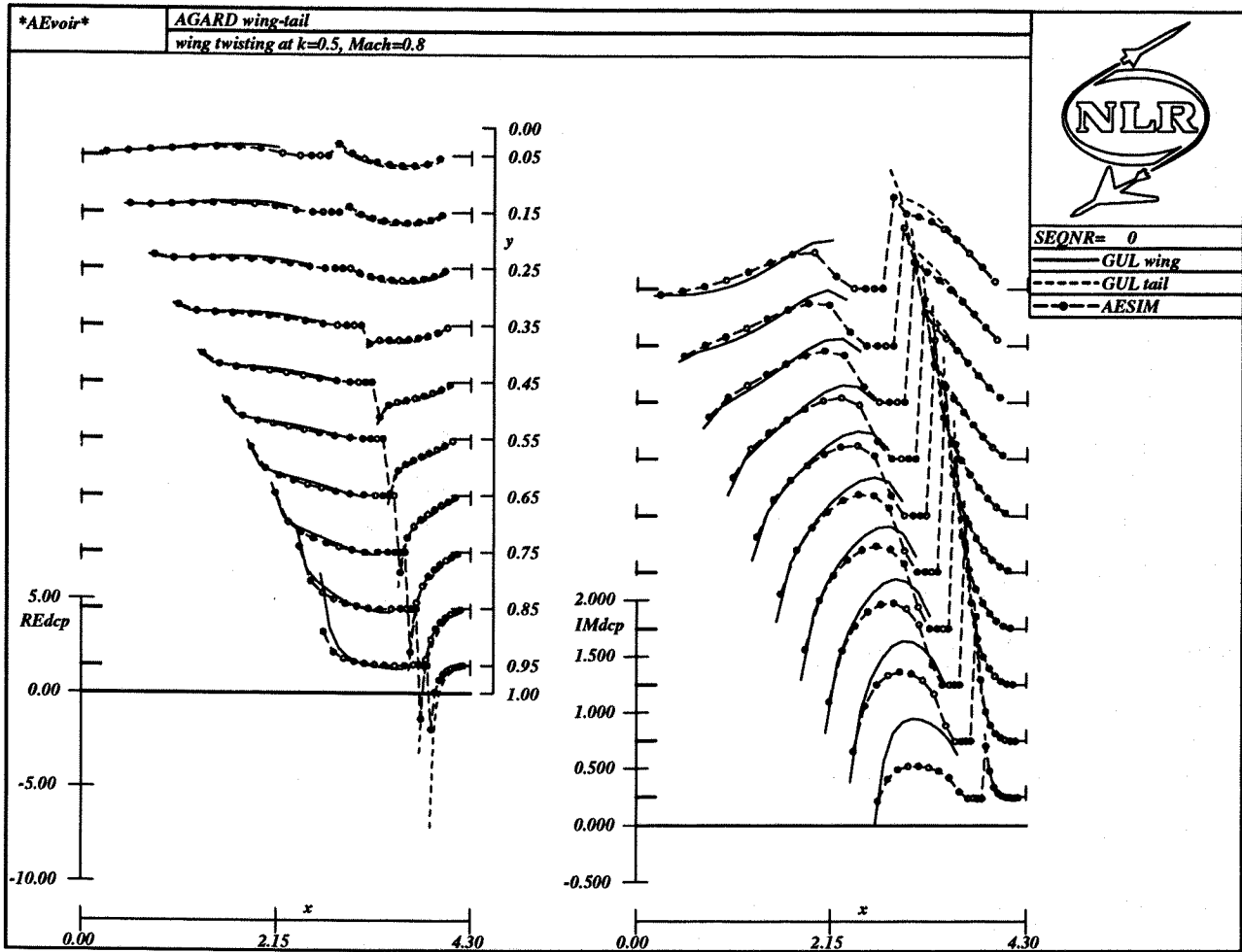
1430

Figure 5: Pressure distribution on wing and tail of AGARD wing-tail configuration

- The interference effects are correctly modeled.

- The differences are attributed to the coarse grid at the edges and probably nonlinear effects due to the full potential modeling and the cross-velocities.

- The results compare reasonably well, keeping in mind that no effort has been made to adapt (refine) the coarse grid.

The table below shows a comparison of the generalized forces. The 30% discrepancy which shows up is attributed to the coarse grid at the leading edges which is not adapted to the square root singular behavior of the pressure coefficients. Lifting surface methods are implicitly adapted to this kind of behavior. Without doubt by refining the grid the discrepancy disappears. Most probably, by using similar techniques as applied in lifting surface methods with respect to the evaluation of pressure and boundary conditions it is possible to obtain results of equal quality on the current grid.

		AESIM		GUL	
i	j	RE. Q_{ij}	IM. Q_{ij}	RE. Q_{ij}	IM.Q_{ij}
1	1	-.07	0.08	-.10	0.12
2	1	0.28	0.15	0.36	0.22
3	1	-.34	0.13	-0.44	0.15
4	1	-.19	0.02	-0.25	0.01

Davies T-tail model

In order to demonstrate the ability of the system to deal with concave surfaces and anti-symmetric modes the Davies T-tail configuration [21] without any ground effect has been considered. The grid is depicted in figures 6-7 and shows the abilility of the grid generator to deal with strongly swept wings, non-uniform distributions and the concavity. Also the double valued tip-axis of the tail and the single valued tip-axis of the fin are clearly visible. It should be noted that the
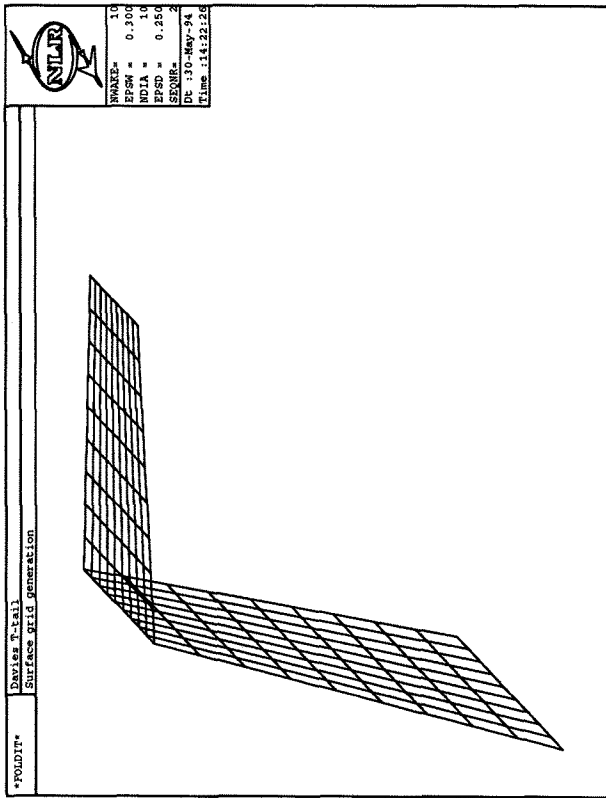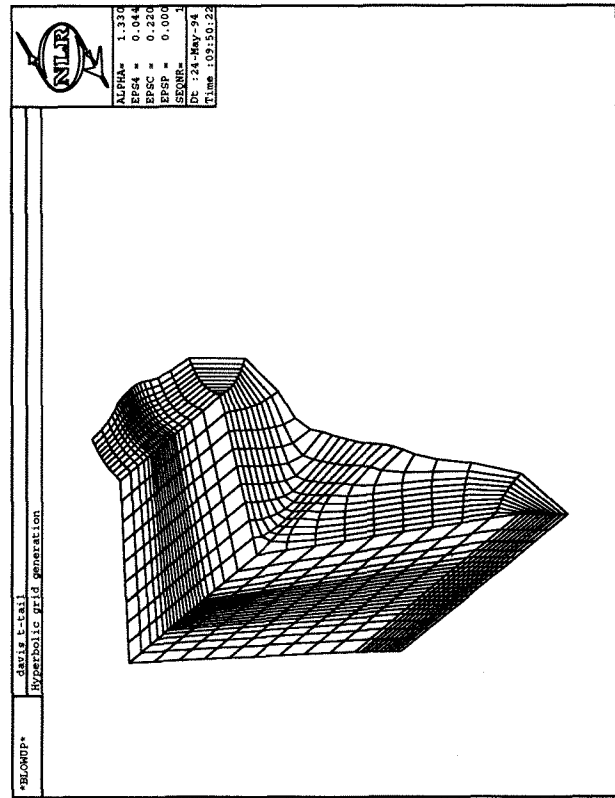
Figure 6: Surface grid of Davies T-tail

Figure 7: Grid around Davies T-tail

coarse distributions on the surfaces are chosen in a way which is acceptable for lifting surface methods. Only 30x29x27 nodes are applied with 10x29 nodes on each side of the surfaces!

Unsteady calculations have been performed at $M_\infty = 0.8$ and k=0.5 in yaw.

Again by a parametric study with respect to the time step and the far field boundaries it was concluded that the application of 256 time steps with 2 subiterations during 3 periods on the current grid results in a 3 digit accuracy.

The geometry of the wing and tail consists of planar quadrilaterals with the following corner co-ordinates:

	fin			tail		
no.	x	y	z	x	y	z
1	0	0	1.5041	0	0	1.5041
2	1	0	1.5041	1	0	1.5041
3	-1.4034	0	0	0.7034	1.2952	1.5041
4	.1007	0	0	1.3676	1.2952	1.5041

The anti-symmetric displacement modes of the configuration are defined as follows:

no	fin h_y	tail h_z	mode
1	1	0	slip
2	x	0	yaw
3	z	y	roll

Figures 8-9 show the first harmonic pressure distributions as calculated with the present method and the GUL method.

The following can be remarked:

- The real part of the AESIM data is in good agreement with the GUL data at both the fin and the tail. A difference is noticable at the fin tip.

- The imaginary part of the AESIM data is in good agreement on the tail and agrees fairly well at the fin. At the tip of the fin the small (Note the difference in scale between the real and imaginary figure) imaginary part on the wing is underpredicted by the AESIM method.

- The interference effects are correctly modeled.

- The differences are attributed to the coarse grid at the edges and the single valued tip-axis applied to the fin in the symmetry plane. Probably nonlinear effects due to the full potential modeling and the cross-velocities may also contribute to the differences.

- The results compare reasonably well, keeping in mind that no effort has been made to adapt (refine) the coarse grid.

The table below shows a comparison of the generalized forces. Again the 30% discrepancy which shows
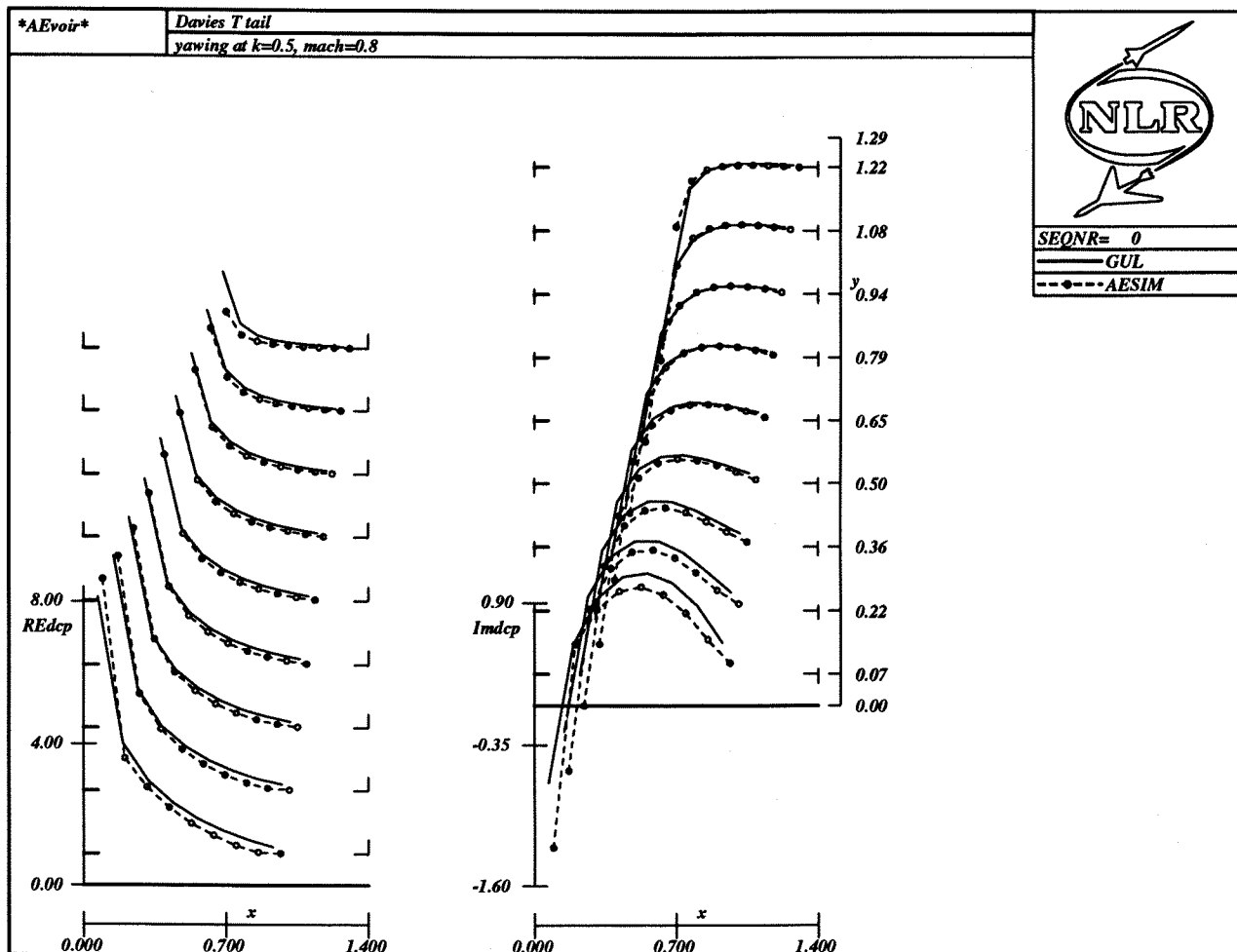
1432

Figure 8: Pressure distribution on tail of Davies T-tail

up is attributed to the coarse grid at the leading edges which is not adapted to the square root singular behavior of the pressure coefficients. The same remarks apply as for the AGARD wing tail application.

		AESIM		GUL	
i	j	RE. Q_{ij}	IM. Q_{ij}	RE. Q_{ij}	IM. Q_{ij}
1	2	2.14	0.47	2.64	.75
2	2	-0.56	0.22	-0.76	.33
3	2	1.34	0.46	1.52	.68

Supercritical transport wing model

The applicability of the AESIM method in flutter analysis is presented for a large aspect ratio supercritical wing which was extensively wind tunnel tested at NLR [22] for the verification of transonic calculation methods. Six conditions were selected for comparing: $M_\infty =$

$0.6, 0.7, 0.75$ and $\alpha = -1\ deg, 2\ deg$. The planform of the wing and the two vibration modes (a fundamental torsion and bending) are shown in figure 10. A grid has been applied with 73x24x27 nodes and is shown in figure 11.

The planform of the wing consists of 2 planar quadrilaterals with the following corner co-ordinates:

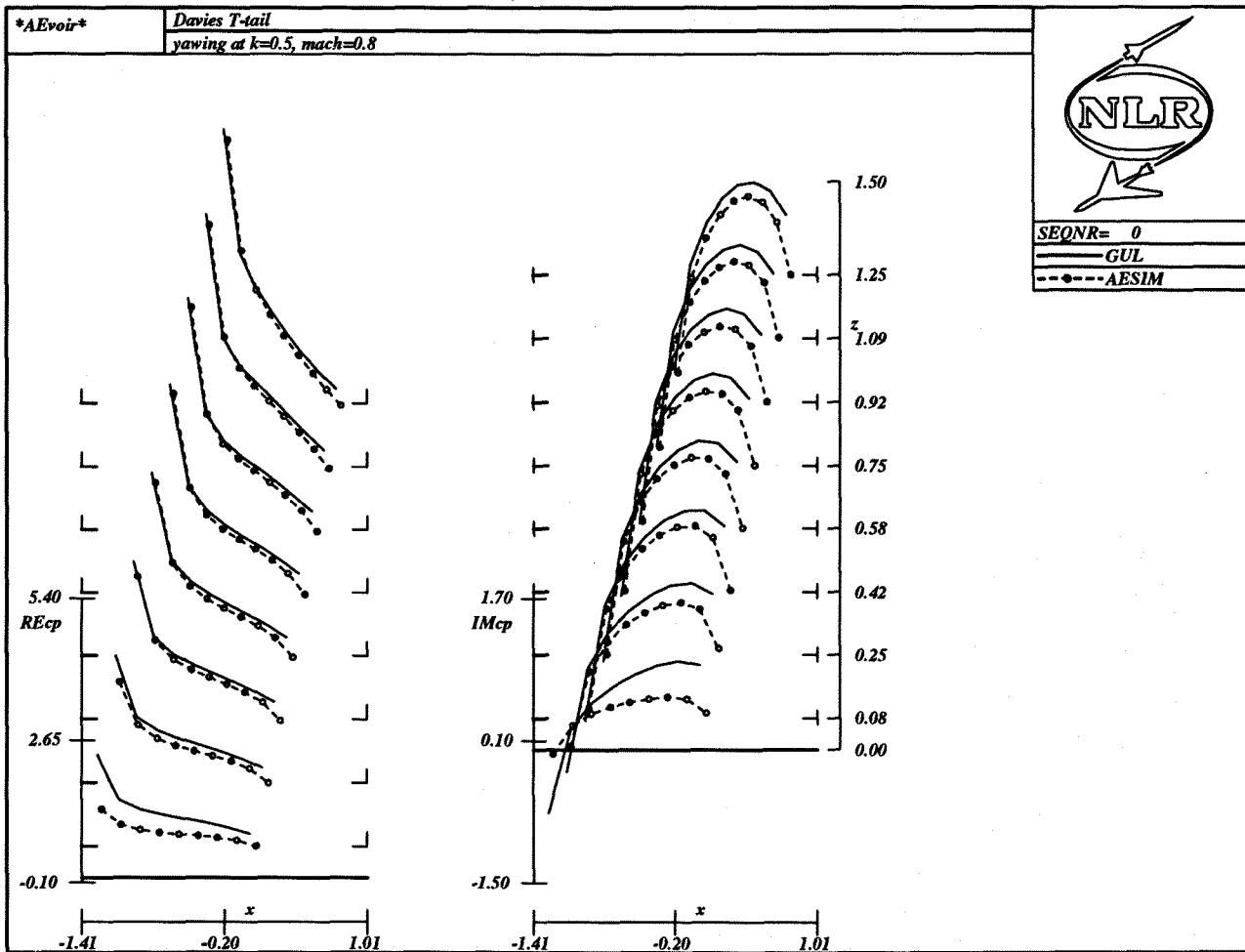| wing vertex	x	y	z
1	0	0	0
2	.193	0	0
3	.0543	.128	0
4	.1933	.128	0
5	.2003	.563	0
6	.2538	.563	0

The displacement modes of the configuration are de-

Figure 9: Pressure distribution on fin of Davies T-tail

fined by the polynomial:

$$h_z = \sum_{i=0}^{1} \sum_{j=0}^{4} v_{ij} x^i y^j, \qquad (87)$$

where the v coefficients are defined in the table below:

i	j	bending v	torsion v
0	0	-0.067477	0.30924
1	0	1.3961	-5.0730
0	1	-0.26775	1.7012
1	1	0.479	-0.25867
0	2	1.0074	-5.0448
1	2	0.87922	9.2499
0	3	0.95724	22.225
1	3	12.0	-8.884
0	4	2.4604	-16.252
1	4	-18.664	-0.23246

The remaining model data are:

	bending	torsion
Generalized mass	0.167 kg	0.615 kg
Natural frequency	72.15 Hz	93.17 Hz
Damping (g)	0.18	0.28

Figure 12 shows the steady pressure distribution at the $M_\infty = 0.7, \alpha = 2$ *deg* condition which has a clearly defined transonic signature (off-design condition).

Experience with AESIM has shown that the best way to tackle an aeroelastic problem - not thoroughly investigated and documented by different people before - is to pass three stages:

1. Use a combination of PK-method and linear (e.g. Doublet Lattice (GUL)) aero. This will give a quick global view of the flutter problem and a starting value of the reduced frequency range in which flutter can be expected. An example is

shown in figure 13. The reduced frequency range obtained this way will be used in the next stage.

2. Apply the PK-method with harmonic generalized forces, calculated by AESIM for forced harmonic motion (pulse response or with the diverging rate approach, once available) of the different mode-shapes. Now a more accurate global impression of the flutter characteristics is obtained. An example is shown in figure 14.

3. This flutter diagram will act as a guide line to trace troublesome operational areas and give starting values for the non-linear direct simulation of the aero-structure coupling in AESIM to gain detailed insight in the damping, frequency and amplitude behavior of the construction.
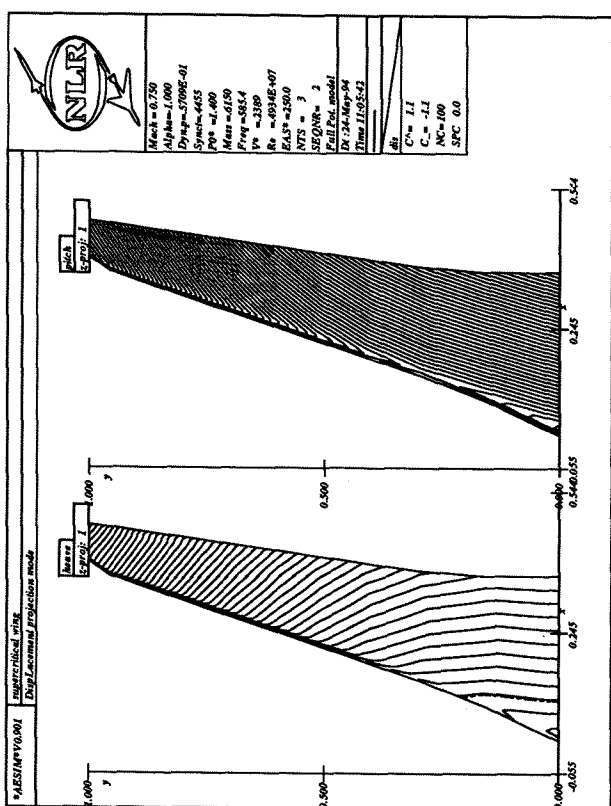
Figure 10: Vibration modes of supercritical wing

The flutter boundaries have been obtained from time response signals of the generalized coordinates, consisting of 2000-2500 time steps. These calculations which have been performed on a 4 R4400 processor SGI ONYX workstation take about 2 hours. A typical example is shown in figure 15. At his request on-line monitoring options provide the user at any time during the simulation process with frequency and damping information of this time response signal, through data fit routines. This way the user controls the process and can stop it at any time to his liking. In order to obtain the flutter boundary for each Mach number
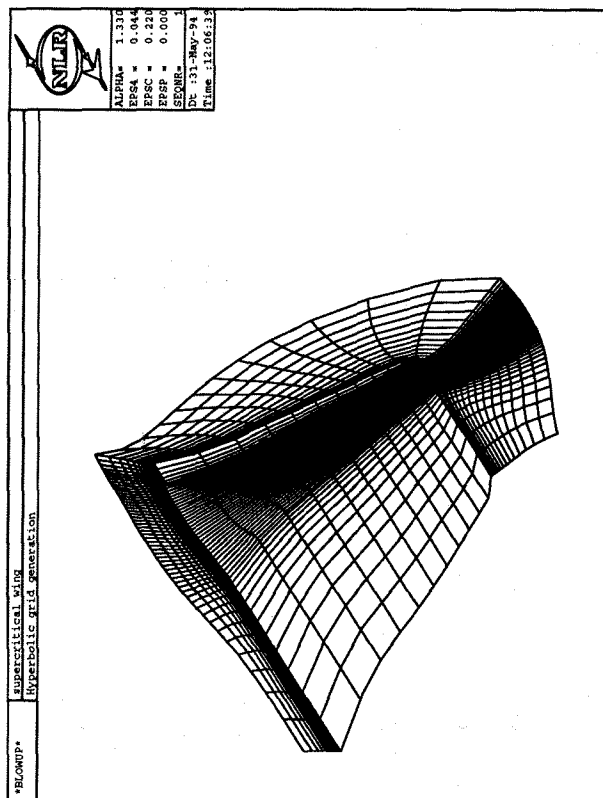

Figure 11: Grid around supercritical wing

an average of 5 dynamic responses needed to be calculated in the present example. From the stage-2 flutter diagram a too high and a too low total pressure were selected. The inbetween flutter boundary was captured in a three-step iteration. Figure 16 shows a comparison of flutter boundaries versus the Mach number. The flutter boundaries are compared for 7 types of results:

1. Experimental data [22], $\alpha = -0.64$ deg, dotted line labeled low. It has been concluded [23], that these data compare best with calculated data at $\alpha = -1.0$ deg.

2. Experimental data [22], $\alpha = 1.78$ deg, dotted line labeled high. It has been concluded [23], that these data compare best with calculated data at $\alpha = 2.0$ deg.

3. Linear theory.

4. FTRAN3, a 3-D transonic method for the steady and unsteady full potential flow about oscillating wings. $\alpha = -1.0$ deg, triangle symbol.

5. FTRAN3, $\alpha = 2.0$ deg, square symbol.

6. Direct simulation data of the current AESIM method, $\alpha = -1.0$ deg, dot symbol.

7. Direct simulation data of the current AESIM method, $\alpha = 2.0$ deg, cross symbol.
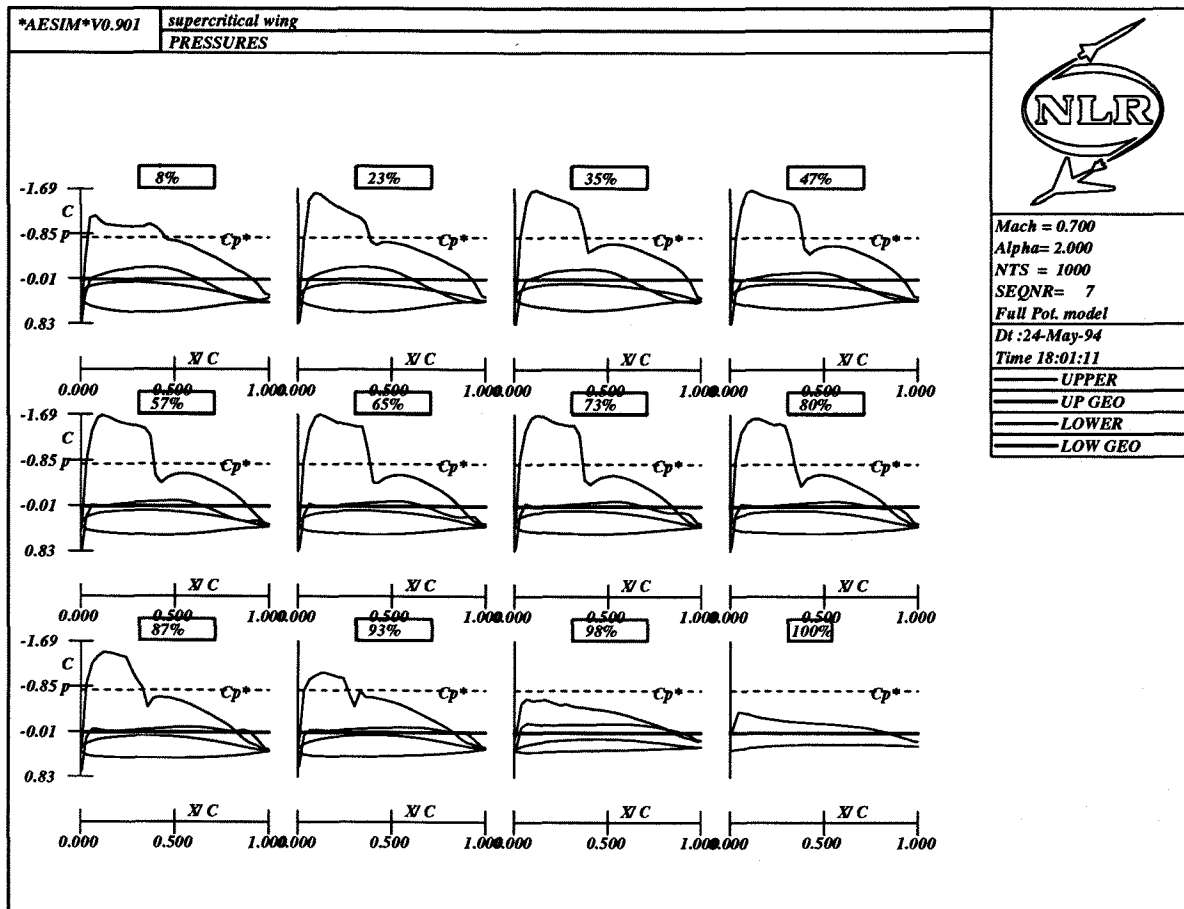
1435

Figure 12: Pressure distribution on supercritical wing

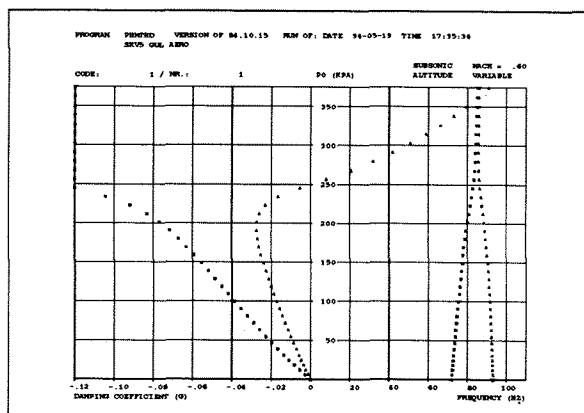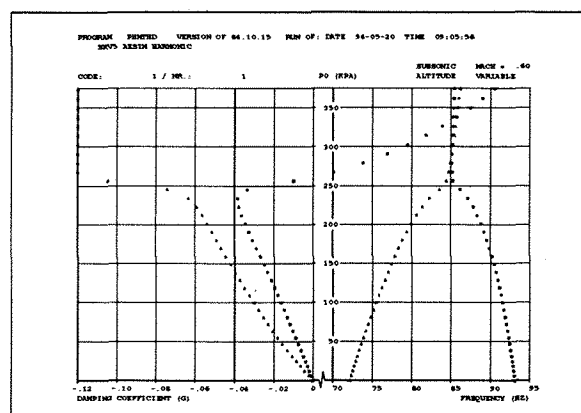Figure 13: Flutter diagram at $M_\infty = 0.6$ for supercritical wing, GUL loads

Figure 14: Flutter diagram at $M_\infty = 0.6, \alpha = 2\ deg$ for supercritical wing, AESIM loads

1436

The following conclusions are drawn:

1. The AESIM results underestimate the time-linearized FTRAN3 results.

2. The AESIM results are conservative compared to the experiment.

3. The minimum values of the double dipped experimental data are fairly well estimated by AESIM.

3-D AGARD standard aeroelastic wing

As a final example results are included of an aeroelastic investigation which was conducted for one of the 3-D AGARD standard aeroelastic configurations in subsonic, transonic and supersonic flow. This configuration is described in [24]. The configuration for dynamic response I wing 445.6 model "weakened no. 3" was selected. The mode shapes and the planform are depicted in figure 17. A grid has been applied with 83x24x27 nodes.

Figure 18 shows a comparison of flutter boundaries versus the Mach number for the test case of several models which were compiled from the literature. The flutter boundaries are compared for seven types of results:

1. Experimental data [24];

2. Lifting surface data [6];

3. Diverging rate FTRAN3 data [6];

4. Time linearized data of Wong as estimated from [26];

5. Direct simulation CAP-TSD data as estimated from [25];

6. Direct simulation data of Knott as estimated from [27];

7. Direct simulation data of the current AESIM method.

The following can be remarked:

1. All methods show a strong transonic dip.

2. The lifting surface data overestimate in the whole Mach range the flutter boundaries as compared to the experiment.

3. The diverging rate FTRAN3 data agree fairly well.

4. The time linearized Wong data agree at the lower and at the higher Mach number, not inbetween.

5. The direct simulation data of Knott is a way off.

6. the AESIM data are in fairly good agreement, except at the lower Mach number.

7. The CAP-TSD data is in good agreement with the experiment.

8. At the subsonic Mach number the differences are larger as compared with the transonic differences. This is of course surprising.

9. The gap between the experiment and the lifting surface data has about the same width as the difference between the transonic methods!

In conclusion:

- For this relatively simple test case the differences between the available results are too large (5%), especially in the subsonic region.

- A probable cause is the applied gas model of the wind tunnel which has to be taken into account when the calculated data do not match the exact experimental mass ratio condition.
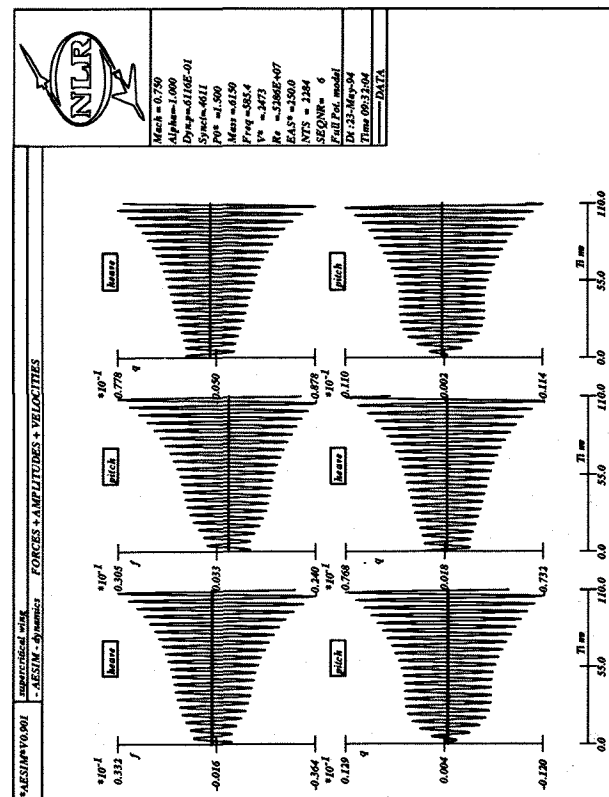

Figure 15: Typical dynamic response at $M_\infty = 0.75, \alpha = -1$ deg for supercritical wing, AESIM loads
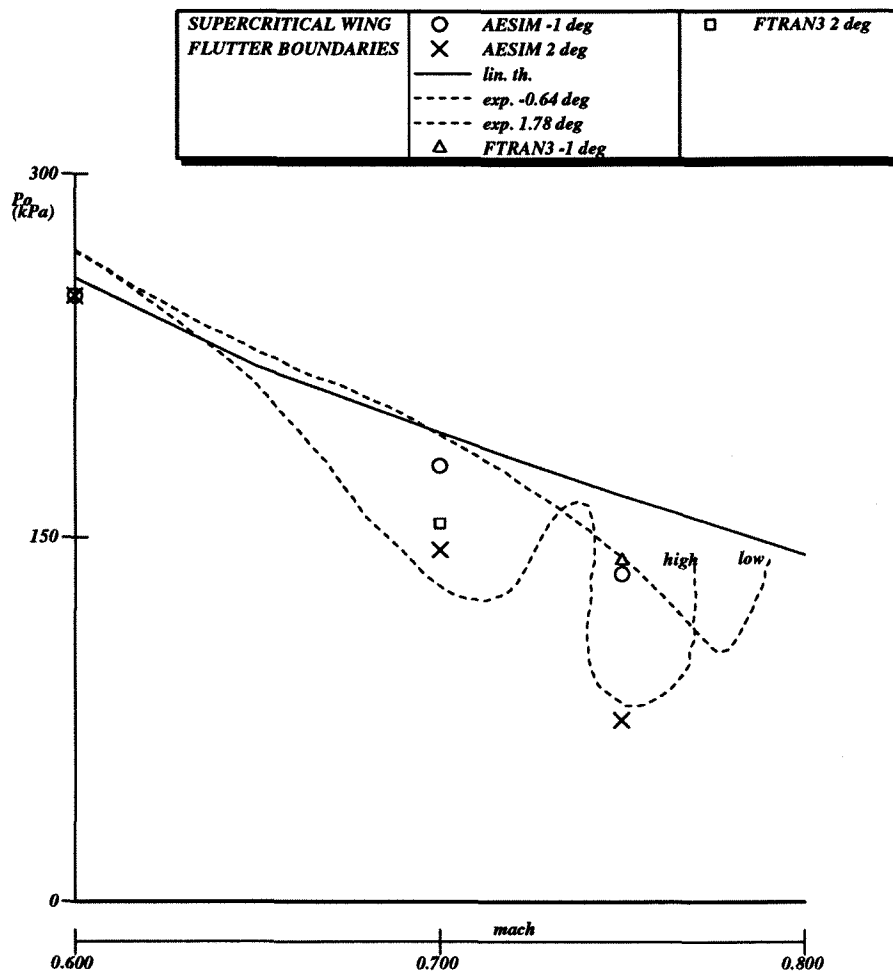
Figure 16: Comparison of calculated flutter boundaries supercritical wing

Conclusion

In this paper the status of the NLR system for aeroelastic simulation has been presented and demonstrated.

Attention has been given to an appropriate beginning of the applied Newton subiteration process.

Extensions of the planar surface spline method to a nonplanar surface spline and volume spline method have been described.

The applications have led to the following results:

- The system is able to predict aeroelastic quantities of interest for non-trivial configurations such as T-tails and wing-tails.

- Flutter boundaries can be obtained by the system for supercritical wings in acceptable turn-around times on current workstations.

- Flutter boundaries compare fairly well with data provided by other methods.

- Except for the PK and GUL applications, no need has shown up for using computer tools outside the current system.

Acknowledgement

Special thanks are due to Professor R.J. Zwaan for his contributions.

References

[1] W. P. Rodden, J. P. Giesing and T. P. Kalman .New developments and applications of the subsonic doublet lattice methods for non-planar configurations, AGARD CP-80-71, Part 2, No. 4, 1971.

*AESIM*V0.901 agard wing 446.5
DispLacement projection mode

-1
z-proj: 1

-2
z-proj: 1

-3
z-proj: 1

-4
z-proj: 1

Mach = 0.901
Alpha= 0.000
Red.f=.2727
NTS = 3
SEQNR= 2
Full Pot. model
Dt :06-Apr-94
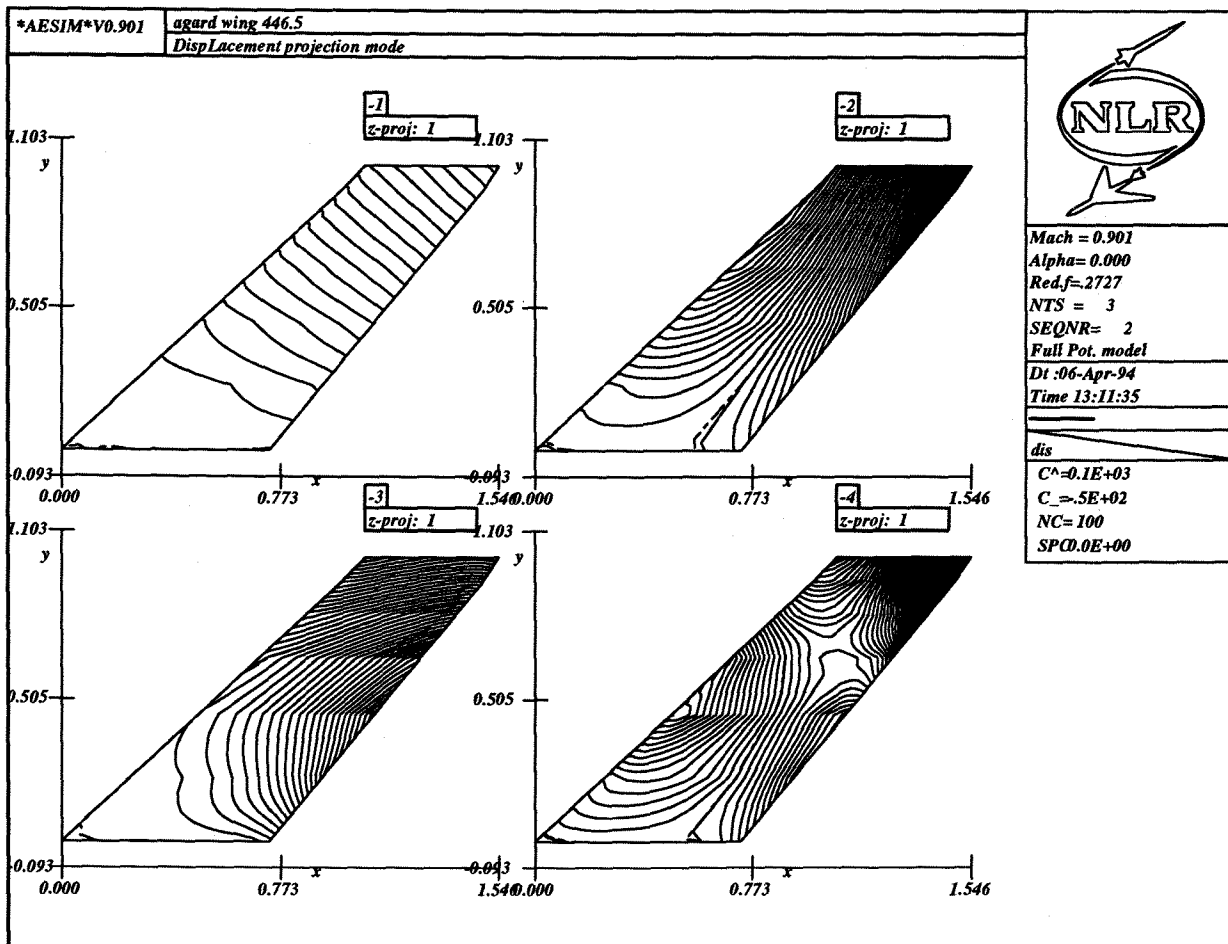Time 13:11:35

dis
C^=0.1E+03
C_=.5E+02
NC= 100
SP(0.0E+00

Figure 17: Vibration modes of wing 445.6

[2] K. Appa and M.J.C. Smith .*Evaluation of the constant pressure panel method (CPM) for unsteady airloads prediction*, AIAA Paper 88-2282, April 1988.

[3] M. H. L. Hounjet .*Calculation of unsteady subsonic and supersonic flow about oscillating wings and bodies by new panel methods*, NLR TP89119 U, April 1989.

[4] M. H. L. Hounjet .*Application of diverging motions to calculate loads for oscillating motions*, AIAA Journal, Vol. 24, No. 10, October 1986, pp 1723-1725 also as *How to make your aerodynamics in flutter calculations cheaper*, NLR MP 85056 U, August 1985.

[5] M. H. L. Hounjet and B. J. G. Eussen.*Beyond the frequency limit of time-linearized methods*, NLR TP91216 U, June 1991.

[6] M.H.L.Hounjet and B.J.G.Eussen .*Prospects of time-linearized unsteady calculation methods for exponentially diverging motions in aeroelasticity* AIAA paper 92-2122, April 1992.

[7] J. Westland and M.H.L. Hounjet, *Clebsch variable model for unsteady, inviscid, transonic flow with strong shock waves*, AIAA 93-3025, July 1993.

[8] H. Ide and V. J. Shankar, *Unsteady full potential aeroelastic computations for flexible configurations*, AIAA paper No. 87-1238, 1987.

[9] J. T. Batina, D. A. Seidel, S. R. Bland and R. M. Bennett, *Unsteady transonic flow calculations for realistic aircraft configurations*, Journal of aircraft, Vol. 26, No. 2, pp 131-139, 1989.

[10] M. H. L. Hounjet, *Hyperbolic grid generation with BEM source terms*, NLR TP 90334 U , October 1990 also in Proceedings IABEM-90, Springer Verlag.
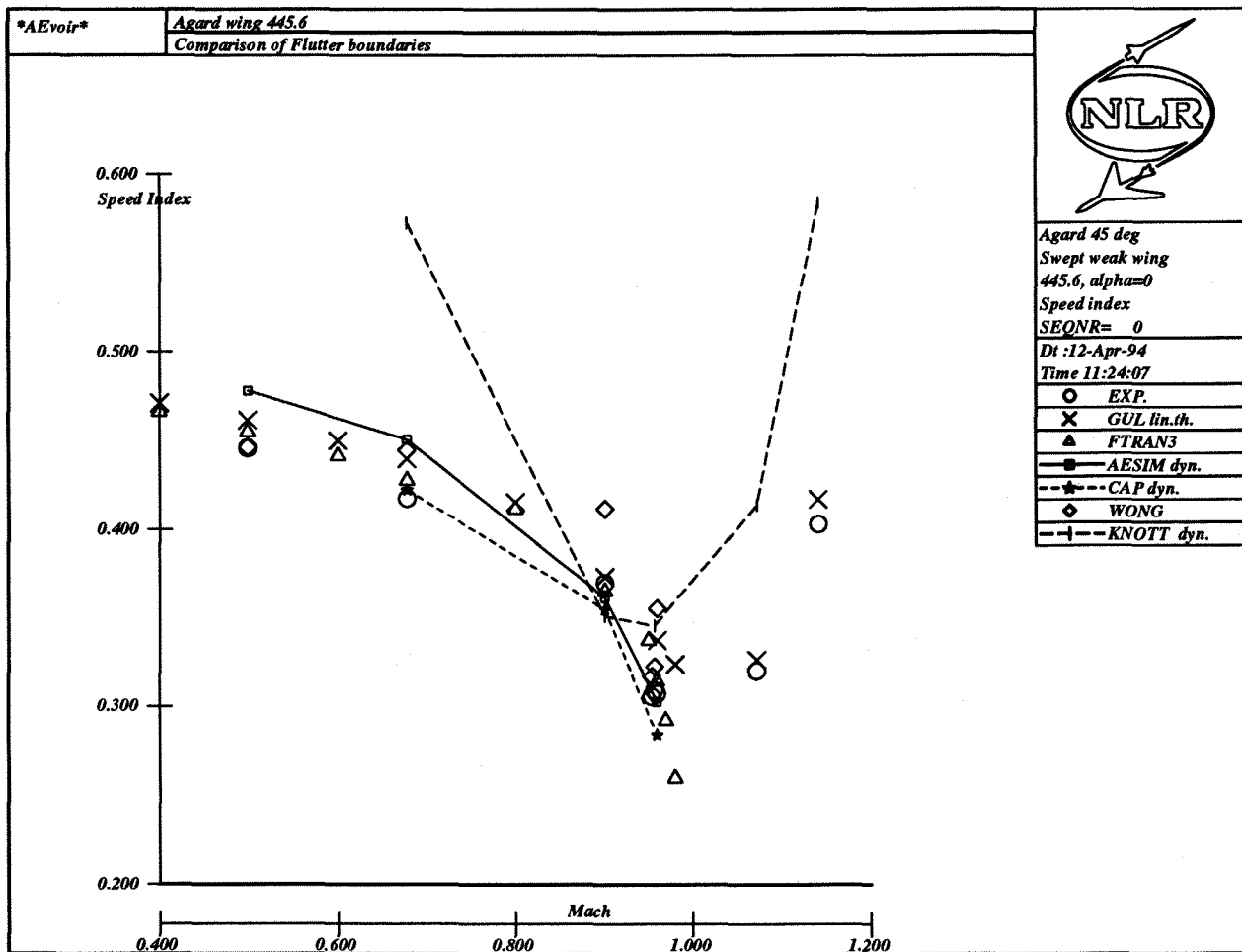
Agard wing 445.6
Comparison of Flutter boundaries

0.600
Speed Index

0.500

0.400

0.300

0.200

Mach
0.400   0.600   0.800   1.000   1.200

Agard 45 deg
Swept weak wing
445.6, alpha=0
Speed index
SEQNR=   0
Dt :12-Apr-94
Time 11:24:07

O	EXP.
X	GUL lin.th.
▲	FTRAN3
■	AESIM dyn.
★	CAP dyn.
◇	WONG
┥	KNOTT dyn.

Figure 18: Flutter boundaries of wing 445.6

[11] M. H. L. Hounjet, *Hyperbolic grid generation control by panel methods*, NLR TP 91061 U, June 1991.

[12] W.M. Chan and J.L. Steger.*A generalised scheme for three-dimensional hyperbolic grid generation* , AIAA-91-1588-CP, July 1991.

[13] R.L.Harder and R.N.Desmarais.*Interpolation using surface splines*, J. of Aircraft, Vol.9, No.2, Feb. 1972, pp. 189-191.

[14] J. F. Thompson. *A general three-dimensional elliptic grid generation system on a composite block-structure*, Computer Methods in applied Mechanics and Engineering, Vol. 64, pp 377-411, 1987

[15] J.J. Alonso and A. Jameson. *Fully-implicit time-marching aeroelastic solutions* , AIAA-94-0056, January 1994.

[16] B. Prananta *Personal Communications*

[17] M.D. Gibbons.*Extending a transonic small disturbance code to treat swept vertical surfaces* , AIAA-92-2503, April 1992.

[18] H. Schippers, *TULIPS: a method to calculate transonic flow about oscillating airfoils*, NLR TR 88193 U, 1988.

[19] A. Jameson and D. A. Caughey, *A finite volume method for transonic potential flow calculations*, AIAA paper 77-635, June 1977.

[20] J. Westland and M.H.L. Hounjet.*Mathematical model of the 3-D unsteady aerodynamic simulation method UENS* NLR CR94???, to appear in 1994.

[21] D.E. Davies .*Theoretical determination of subsonic oscillatory airforce coefficients for fin-tailplane configurations* RAE TR 79125, september 1979.

[22] A.J. Persoon, J.J. Horsten and J.J. Meijer, On measuring transonic dips in the flutter boundaries

of a supercritical wing in the wind tunnel, AIAA-83-1031, May 1983.

[23] M. H. L. Hounjet , J Th. van der Kolk and J.J. Meijer .*Application of NLR's calculation methods to transonic flow about oscillating wings*, Journal of Aircraft, Vol.22, No. 12, December 1985, pp 1034-1042.

[24] E. C. Yates, Jr. .*AGARD standard aeroelastic configurations for dynamic reponse, I-wing 445.6*, AGARD report No.765, July 1988.

[25] R. M. Bennett and J. T. Batina .*Application of the CAP-TSD unsteady transonic small disturbance program to wing flutter*, Proceedings European Forum on Aeroelasticity and Structural Dynamics 1989, DGLR Bericht 89-01, paper no. 89-003, pp. 25-34

[26] Y.S. Wong, B.H.K. Lee and H.S. Murty. *A time-linearization approach for unsteady transonic flows* , AGARD CP 507, pp 6.1-6.22, March 1992.

[27] M.J. Knott. *Transonic aeroelastic calculations in both the time and frequency domain* , AGARD CP 507, pp 15.1-15.8, March 1992.